Journal of Volcanology and Geothermal Research 259 (2013) 248–269

Contents lists available at SciVerse ScienceDirect

Journal of Volcanology and Geothermal Research

journal homepage: www.elsevier.com/locate/jvolgeores

# High-resolution satellite and airborne thermal infrared imaging of precursory unrest and 2009 eruption at Redoubt Volcano, Alaska

Rick L. Wessels [a,*], R. Greg Vaughan [b], Matthew R. Patrick [c], Michelle L. Coombs [a]

[a] Alaska Volcano Observatory, U.S. Geological Survey, 4200 University Drive, Anchorage, AK, United States
[b] Astrogeology Science Center, U.S. Geological Survey, 2255 N. Gemini Drive, Flagstaff, AZ, United States
[c] Hawaiian Volcano Observatory, U.S. Geological Survey, PO Box 51, Hawai'i National Park, HI, United States

ARTICLE INFO

*Article history:*
Received 23 June 2011
Accepted 3 April 2012
Available online 13 April 2012

*Keywords:*
ASTER
Landsat
Thermal infrared
Lava dome
FLIR
Redoubt Volcano

ABSTRACT

A combination of satellite and airborne high-resolution visible and thermal infrared (TIR) image data detected and measured changes at Redoubt Volcano during the 2008–2009 unrest and eruption. The TIR sensors detected persistent elevated temperatures at summit ice-melt holes as seismicity and gas emissions increased in late 2008 to March 2009. A phreatic explosion on 15 March was followed by more than 19 magmatic explosive events from 23 March to 4 April that produced high-altitude ash clouds and large lahars. Two (or three) lava domes extruded and were destroyed between 23 March and 4 April. After 4 April, the eruption extruded a large lava dome that continued to grow until at least early July 2009.

Published by Elsevier B.V.

## 1. Introduction

The Alaska Volcano Observatory (AVO) monitors all North Pacific volcanoes with satellite data including, near-real-time Advanced Very High Resolution Radiometer (AVHRR), Moderate Resolution Imaging Spectroradiometer (MODIS), and Geostationary Operational Environmental Satellites (GOES). These data are received within minutes of acquisition providing high temporal resolution (minutes to hours) at low spatial resolutions of 1–8 km. Several papers in this issue discuss various applications of these data (Webley et al., 2013; Schneider and Hoblitt, 2013). High spatial resolution thermal infrared (TIR) data from several satellites (60–120-m resolution) and forward looking infrared radiometer (FLIR) airborne imaging (1–10-m spatial resolution) have been used to detect and measure volcano thermal features before, during, and after recent eruptions around the globe (Calvari et al., 2005; Vaughan and Hook, 2006; Schneider et al., 2009; Wessels et al., 2010; Spampinato et al., 2011).

Spaceborne TIR remote sensing tools have been used in numerous studies to characterize volcanic thermal features (Oppenheimer, 1993; Flynn et al., 1994; Harris and Stevenson, 1997; Harris et al., 1998, 1999; Wooster et al., 2000; Kaneko et al., 2002; Oppenheimer and Yirgu, 2002; Wright and Flynn, 2003; Lombardo et al., 2004; Patrick et al., 2004; Ramsey and Dehn, 2004; Pieri and Abrams, 2005; Vaughan et al., 2005; Vaughan and Hook, 2006; Davies et al., 2008; Kervyn et al., 2008; Trunk and Bernard, 2008; Carter and Ramsey, 2009, 2010; Coppola et al., 2010; Vaughan et al., 2010). The physical basis for TIR remote sensing, including Planck's (1914) Law and the equations describing TIR radiance measured at the sensor, atmospheric correction, and temperature retrieval, are described in many of the aforementioned papers and their references.

High-resolution TIR data provided critical observations during the precursory unrest and eruption at Redoubt Volcano. From November 2007 through August 2010, a series of 14 FLIR surveys and over 300 satellite TIR and visible/near-infrared (VNIR) scenes were acquired over Redoubt Volcano. These data provided high spatial resolution observations every 1 to 10 days that added important details to more frequent, low-resolution observations from the much larger collection of near-real-time data.

The high-resolution TIR remote sensing response to the 2009 eruption of Redoubt Volcano initially focused on detecting and monitoring changes in possible thermal areas and other surface features to assess the extent of unrest and the likelihood and timing of an eruption. As the eruption commenced, the TIR response changed to measuring and monitoring eruptive products and surveying edifice for new features. During the effusion of lava domes and flows, the TIR data readily identify areas of active lava and gas effusion as well as providing a means to measure dimensions, assess flow structures and surface textures.

## 2. Regional setting

Redoubt Volcano, part of the Aleutian volcanic arc, is located on the west side of Cook Inlet 170 km southwest of Anchorage, Alaska

* Corresponding author.
*E-mail address:* rwessels@usgs.gov (R.L. Wessels).

0377-0273/$ – see front matter. Published by Elsevier B.V.
doi:10.1016/j.jvolgeores.2012.04.014

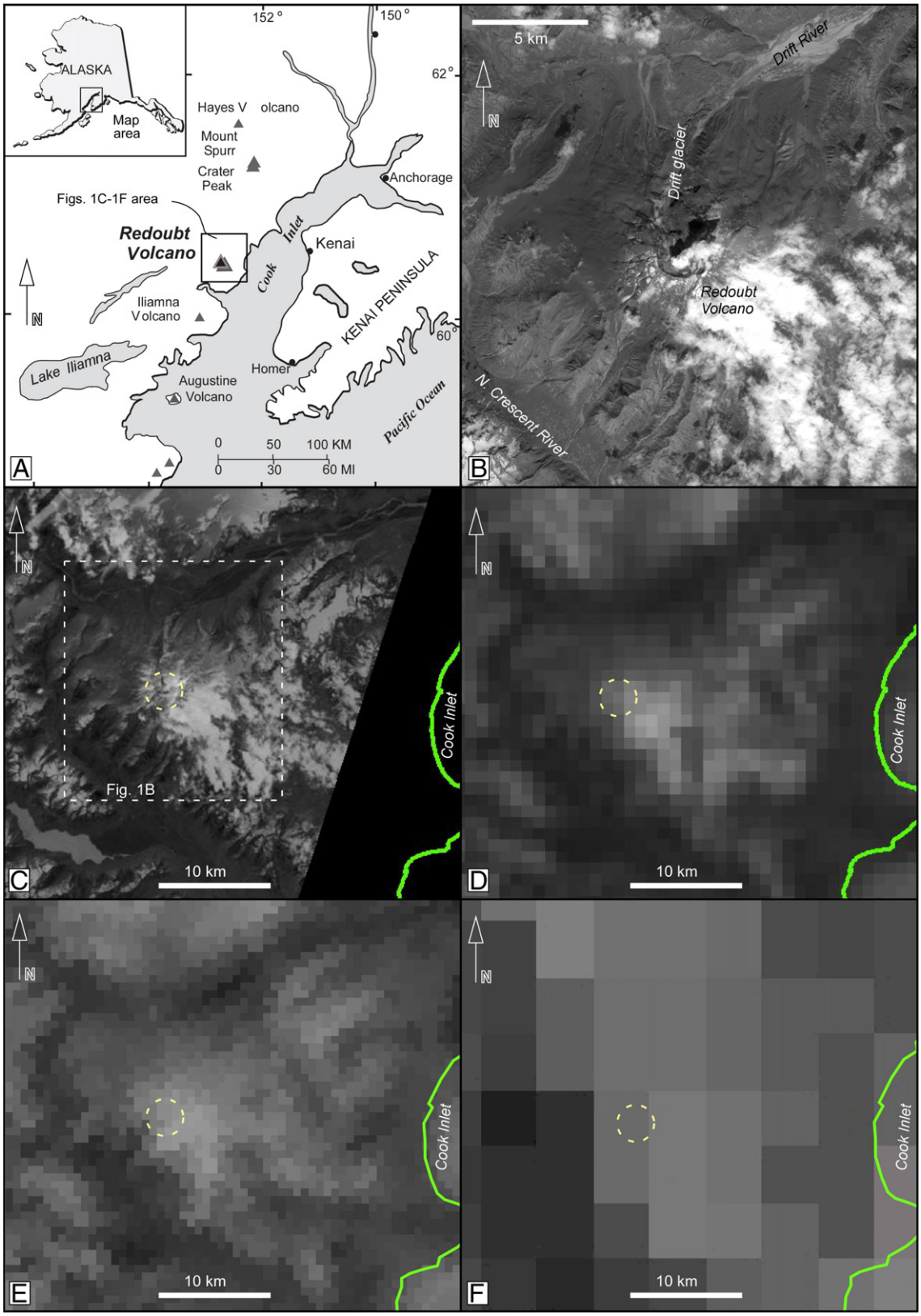


**Fig. 1.** (A) Location map of Redoubt Volcano, Alaska. (B) Subset of 6 June 2009, 21:38 UTC ASTER 15-m VNIR bands 3, 2, and 1 as gray scale showing local features at Redoubt Volcano. Figures C–F compare spatial resolutions of TIR bands (about 11 μm) over Redoubt Volcano from four different sensors acquired during daylight hours between 21:30 and 22:01 UTC on 6 June 2009: (C) ASTER 90-m TIR band 14. White box outlines figure B area, (D) MODIS 1-km TIR band 31, (E) AVHRR 1.1-km TIR band 4, and (F) GOES ~8-km TIR band 4. The dashed circle shows the location of the summit crater area.
After Duda et al. (2009a, 2009b).

**Table 1**
2008–2009 FLIR measurements of temperatures of thermal features and lava dome surfaces at Redoubt Volcano. The italicized-gray rows list temperatures from the upper rubbly facies that began to flow from the apex vent sometime in early May 2009.

| Date | [a]Time UTC | Saturated | [b]$T_{max}$ (°C) | [c]$T_{bg}$ (°C) | DT (°C) | [d]$T_{mean}$ (°C) | [e]$T_{stdev}$ (°C) | Ambient setting $T_{amb}$ (°C) | RH (%) | Wind (kts) | Image location (DS=dome surface, (b) blocky, (u) upper scoriaceous facies) | Observation quality | |
|---|---|---|---|---|---|---|---|---|---|---|---|---|---|
| 2008/11/07 | 20:00:00 | | 20.2 | -19 | 39.2 | 5 | 8 | -13 | 38 | 9 | Ice pit above 89-90 dome viewed from below | Summit ice mostly clear with light steam | Pre-eruption |
| 2009/02/10 | 20:30:00 | | 28.6 | -17 | 45.6 | 10.6 | 5 | -20 | 36 | 10 | 1990 dome rock exposed in Ice pit | Summit ice mostly clear with light steam | |
| 2009/03/31 | 17:45:00 | | 127 | -20 | 147 | 89 | 16 | -24 | 64 | 10 | Part dome view from N, DS relatively smooth | Dome mostly obscured by steam/ash plume | Explosive phase |
| 2009/04/04 | 17:48:00 | | 112 | -10 | 122 | 33 | 13 | -16 | 50 | 15 | DS from N, texture obscured by plume | Dome mostly obscured by steam/ash plume | Effusive phase |
| 2009/04/16 | 22:00:00 | | 430.4 | -15 | 445.4 | 118.5 | 48.6 | -11 | 67 | 12 | DS (b) large, active sloughing area on N face | Most of dome exposed within steam plume | |
| 2009/04/30 | 20:00:00 | | 313.9 | 3 | 310.9 | 64.3 | 27 | -1 | 26 | 30 | DS (b) large, active sloughing area on N face | Mostly clear views with plume | |
| 2009/05/08 | 19:46:00 | | 273 | -3 | 276 | 74.7 | 36 | -7 | 64 | 9 | DS (b) active sloughing area on N face | Mostly clear views with plume | |
| *2009/05/08* | *19:46:00* | | *110* | *-3* | *113* | *20.6* | *6.6* | | | | *DS (u) N of apex* | | |
| 2009/05/16 | 22:45:00 | | 345 | -10 | 355 | 44.5 | 24.2 | -10 | 86 | 8 | DS (b) active sloughing area on N face | Summit partly obscured by light steam/ash | |
| *2009/05/16* | *22:45:00* | | *72* | *-10* | *82* | *31* | *1* | | | | *DS (u) N of apex* | | |
| 2009/06/09 | 21:00:00 | > | 260 | 0 | 260 | 35.2 | 34 | 3 | 41 | 10 | DS (b) S half of dome | Steam obscured portions of dome apex | |
| *2009/06/09* | *21:00:00* | | *34.3* | *0* | *34.3* | *12.8* | *3.1* | | | | *DS (u) N of apex* | | |
| 2009/07/01 | 18:30:00 | > | 260 | 1 | 259 | 20.6 | 9.6 | 2 | 73 | 8 | DS (b) S half of dome | Summit partly obscured by steam + clouds | |
| *2009/07/01* | *18:30:00* | | *30.2* | *1* | *29.2* | *6* | *2.9* | | | | *DS (u) N of apex* | | |
| 2009/08/20 | 18:45:00 | | 363 | 3 | 360 | 15 | 5 | -8 | 29 | 17 | DS (b) S half of dome | Fresh snow has covered many deposits | Post-eruption |
| *2009/08/20* | *18:45:00* | | *43* | *3* | *40* | *7* | *1.1* | | | | *DS (u) N of apex* | | |
| 2009/09/23 | 19:30:00 | | 313.5 | -23 | 336.5 | 5.3 | 18 | -12 | 56 | 3 | DS (b) S half of dome | Very clear summit views; rock sampling | |
| *2009/09/23* | *19:30:00* | | *105* | *-23* | *128* | *-5.7* | *3.3* | | | | *DS (u) N of apex, hot radial fractures* | | |
| 2009/12/31 | 19:00:00 | > | 260 | -15 | 275 | 1.8 | 17.5 | -10 | 72 | 7 | DS (b) S half of dome | Partly cloudy, partly snow-covered dome | |
| *2009/12/31* | *19:00:00* | | *176* | *-15* | *191* | *-6.2* | *4.6* | | | | *DS (u) N of apex, hot radial fractures* | | |
| 2010/08/22 | 5:00:00 | > | 260 | -4.4 | 264.4 | 4 | 13 | -3 | 85 | 7 | DS (b)S half of dome | Partly cloudy, partly snow-covered dome | |
| *2010/08/22* | *5:00:00* | | *120* | *-4.4* | *124.4* | *0.8* | *1.7* | | | | *DS (u) N of apex, hot radial fractures* | | |

[a] Overflight and field work typically span one-plus hours and are generally midday.
[b] ($T_{max}$) FLIR maximum pixel-integrated temperature.
[c] ($T_{bg}$) FLIR mean background temperature.
[d] ($T_{avg}$) FLIRT mean surface temperature of active lava areas.
[e] ($T_{stdev}$) FLIRT temperature range within mean surface.

(Fig. 1). The upper flanks of the 3110 m a.s.l. stratovolcano and its summit crater are usually covered by permanent snow and ice. The Drift Glacier occupies the dominant crater breach and valley on the north side of the volcano. Before 2009, recent historical eruptions occurred in 1965–8 and 1989–90 (Brantley, 1990; Miller, 1994; Miller and Chouet, 1994; Till et al., 1994). Details of the sequence of volcanic deposits and emissions from the 2009 eruption are described in several papers in this issue (see Bull and Buurman, 2013; Bull et al., 2013; Coombs et al., 2013; Wallace et al., 2013).

## 3. Methods

This paper features observations from both spaceborne and airborne high-resolution TIR sensors with a few VNIR images included for context. While the high-resolution observations were not nearly as frequent as the low-resolution meteorological satellite observations, the 1–120-m spatial resolution of these data offer unique views of small-scale changes and features. The airborne and satellite imaging described in this paper focuses primarily on the period from November 2007 to August 2009. During that time, high resolution satellite sensors used in this work acquired more than 230 day and night TIR images with 60–120-m resolution and more than 80 airborne TIR, commercial visible to near-infrared (VNIR) and synthetic aperture radar (SAR) images with 0.5–4-m resolution (Appendix 1).

### 3.1. Airborne and ground-based FLIR thermal infrared images

Fourteen FLIR surveys conducted between 7 November 2008 and 21 August 2010 showed areas of heating and melting in the summit crater beneath the glacial ice before the first explosive events, highlighted thermal structures within the domes and talus, and revealed evolution of the growing dome and cooling once extruded. FLIR data were acquired during helicopter flights as weather and volcanic activity permitted (Appendix 1 and Table 1).

Both airborne surveys and repeat ground-based time-lapse thermal infrared sequences were acquired using FLIR Systems ThermaCAM PM595 and ThermaCAM S40 cameras. The cameras employ a 320× 240 microbolometer detector array sensitive to thermal infrared emissions from 7.5 to 13 μm. Both systems used a 24° lens with a horizontal field of view of 420 m and a pixel resolution of 1.3 m at a distance of 1 km. The majority of observation distances of each survey ranged from 1 to 5 km, averaging about 1.6 km from the sensor to target. Both FLIRs can record temperatures from −40 to 1500 °C using one of three preset calibration ranges: −40–120 °C, 80–500 °C (0–500 °C for the S40), and 350–1500 °C. FLIR surveys were collected in the two lower temperature settings since the surface temperatures at Redoubt Volcano ranged from typical Alaska winter low ambient temperatures <−30 °C to small, hot volcanic features such as fumaroles and lava dome fractures >400 °C.

The at-sensor-radiance is converted to temperature-at-surface for each pixel by making a first-order correction for atmospheric absorption, surface material emissivity and ambient temperature. The atmospheric correction depends on input of a distance to target, ambient air temperature, relative humidity, and reflected temperature from other sources. Careful analyses must also account for TIR absorption from volcanic steam and gas, variable surface textures and compositions, and oblique viewing geometries (Harris et al., 2005; Ball and Pinkerton, 2006; Sawyer and Burton, 2006; Schneider et al., 2009; Spampinato et al., 2011). Air temperature and humidity were measured at the sensor location during each flight and compared with Global Data Assimilation System (GDAS1) Archive interpolated model soundings at the volcano. The distance to target was calculated from the difference between the time-synced GPS helicopter position (x,y,z) and the estimated position of the target feature. Repeating measurements from multiple viewing angles and avoiding areas of high gas and steam emissions minimized errors.

In the low range setting of the PM595, temperatures above the calibrated maximum of 120 °C did not actually saturate the detector until about 270 °C at the typical distance and atmosphere conditions for these surveys. Calibrated blackbody measurements suggest that errors in the recorded temperature above the calibrated range will be less than errors introduced by volcanic fume and poorly constrained atmospheric correction and oblique image geometry assumptions.

The FLIR image color scales presented in the following sections represent a linear scaling of 98% of the data clipping the lowest values to black and the highest to white. All dates and times are listed in UTC unless otherwise specified.

### 3.2. High resolution satellite data

#### 3.2.1. ASTER

The Advanced Spaceborne Thermal Emission and Reflection Radiometer (ASTER) acquired most of the high-resolution satellite-based TIR data used for this study. The ASTER instrument is mounted on the Terra spacecraft, launched in 1999. ASTER measures top-of-atmosphere radiance in 14 spectral channels: three VNIR channels at 15-m per pixel; six SWIR channels at 30-m per pixel; and five TIR channels at 90-m per pixel (Yamaguchi et al., 1998). The six SWIR channels have been non-operational since 2008 due to degradation of the detector cooler system. Each ASTER image covers a 60×60 $km^2$ area.

An automated rapid response system that automates much of the acquisition scheduling is one of the unique characteristics of ASTER.

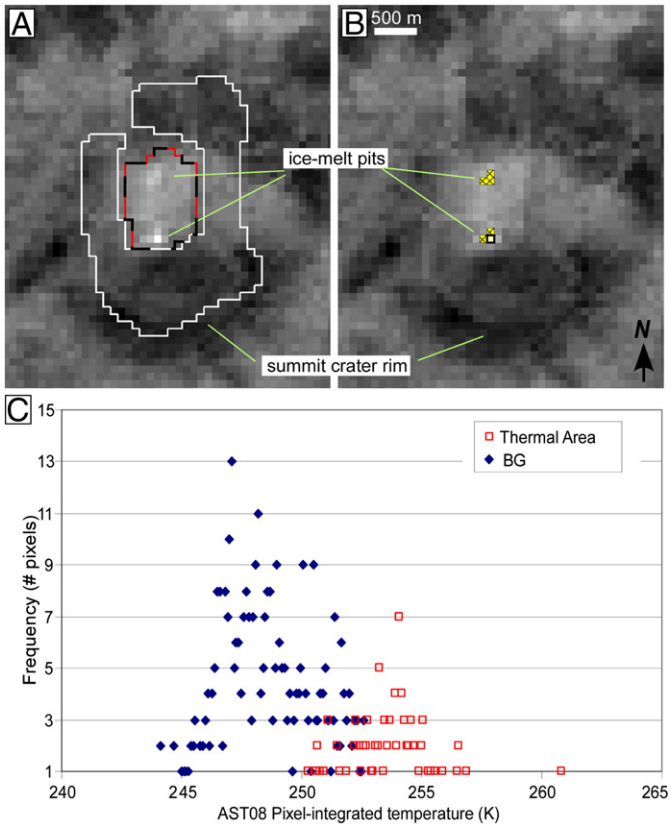


**Fig. 2.** (A) ASTER nighttime temperature image from 10 January 2009 showing a subtle thermal anomaly (a few bright pixels relative to surroundings). The inner dashed line outlines the crater area evaluated for thermal anomalies. Area in white is the surrounding background (BG) area to which the crater area was compared. (B) The five pixels in cross-hatch pattern are all the pixels in the thermal area that are >4 standard deviations above the mean of the BG area. The single hottest pixel is outlined in black. (C) Pixel count of pixel-integrated AST08 temperatures in each area.

**Table 2**
2008–2009 ASTER TIR temperatures. $PIT_{max}$ Hot 1 = maximum pixel-integrated temperature, $PIT_{max}$ SD = one standard deviation of $PIT_{max}$, and $BG_{Mean}$ = mean background temperature.

| Date | Day /night | $PIT_{max}$ Hot 1 (K) | $PIT_{max}$ SD | $BG_{Mean}$ (K) | ΔT | #Pixels > $BG_{Mean}$ + 3SD | #Pixels > $BG_{Mean}$ + 4SD | Geothermal Rad Emit Hot 1 ($W/m^2$) | Geothermal Rad GHF Hot 1 (MW) | Highest sub-pixel temps (K) | Highest sub-pixel temps (C) | error (+/−) | Area of highest sub-pixel temp ($m^2$) | error (+/−) | |
|---|---|---|---|---|---|---|---|---|---|---|---|---|---|---|---|
| 2008/02/02 | n | 252.0 | 1.4 | 244.7 | 7.3 | 4 | 1 | 24.69 | 0.20 | | | | | | |
| 2008/02/25 | n | 257.0 | 2.6 | 247.8 | 9.2 | 0 | 0 | 32.37 | 0.26 | | | | | | |
| 2008/03/03 | n | 259.0 | 1.4 | 253.5 | 5.5 | 2 | 0 | 20.23 | 0.16 | | | | | | |
| 2008/03/26 | n | 256.0 | 2.2 | 249.5 | 6.5 | 0 | 0 | 22.90 | 0.19 | | | | | | |
| 2008/04/13 | n | 258.5 | 1.8 | 253.5 | 5.0 | 0 | 0 | 18.52 | 0.30 | | | | | | |
| 2008/04/29 | n | 257.5 | 1.5 | 252.1 | 5.4 | 0 | 0 | 19.56 | 0.16 | | | | | | |
| 2008/06/07 | n | 268.5 | 1.0 | 265.0 | 3.5 | 1 | 0 | 14.52 | 0.12 | | | | | | |
| 2008/06/09 | n | 272.3 | 1.9 | 266.2 | 6.1 | 0 | 0 | 26.31 | 0.21 | | | | | | |
| 2008/07/11 | n | 273.7 | 1.0 | 270.7 | 3.0 | 0 | 0 | 13.10 | 0.42 | | | | | | |
| 2008/08/03 | n | 275.5 | 1.6 | 270.3 | 5.2 | 0 | 0 | 23.17 | 0.19 | | | | | | |
| 2008/08/10 | n | 272.5 | 2.1 | 266.1 | 6.4 | 2 | 0 | 27.27 | 0.44 | | | | | | |
| 2008/10/13 | n | 260.0 | 2.4 | 250.6 | 9.4 | 0 | 0 | 34.48 | 0.28 | 363 | 89 | 9 | 150 | 46 | Pre-eruption |
| 2008/10/16 | d | 264.1 | 1.5 | 256.7 | 7.4 | 0 | 0 | 28.70 | 0.23 | 291 | 18 | 44 | 583 | 87 | |
| 2008/10/29 | n | 258.9 | 1.0 | 252.2 | 6.7 | 7 | 1 | 24.50 | 0.20 | 401 | 128 | 54 | 97 | 69 | |
| 2008/11/01 | d | 260.9 | 1.7 | 254.5 | 6.4 | 0 | 0 | 24.14 | 0.20 | 312 | 48 | 48 | 122 | 18 | |
| 2008/11/14 | n | 259.3 | 1.3 | 253.0 | 6.3 | 24 | 0 | 23.42 | 0.19 | | | | | | |
| 2008/12/16 | n | 262.8 | 1.2 | 254.4 | 8.4 | 3 | 1 | 31.90 | 0.26 | 351 | 78 | 6 | 253 | 72 | |
| 2009/01/10 | n | 260.8 | 1.6 | 248.7 | 12.1 | 22 | 5 | 44.14 | 0.36 | 315 | 42 | 21 | 795 | 449 | |
| 2009/01/26 | n | 261.5 | 2.2 | 250.6 | 10.9 | 13 | 1 | 39.95 | 0.32 | 360 | 87 | 5 | 243 | 17 | |
| 2009/02/02 | n | 252.7 | 2.4 | 241.4 | 11.3 | 83 | 59 | 37.66 | 0.31 | 412 | 139 | 62 | 75 | 11 | |
| 2009/02/14 | d | 264.4 | 1.6 | 256.8 | 7.6 | 7 | 5 | 29.71 | 0.24 | 351 | 78 | 30 | 228 | 101 | |
| 2009/02/27 | n | 265.1 | 3.6 | 251.4 | 13.7 | 80 | 59 | 51.97 | 0.42 | 328 | 55 | 49 | 578 | 87 | |
| 2009/03/02 | d | 263.8 | 2.0 | 253.6 | 10.2 | 11 | 8 | 39.01 | 0.32 | 344 | 71 | 20 | 486 | 161 | |
| 2009/03/24 | n | 260.4 | 1.9 | 249.8 | 10.6 | 201 | 148 | 38.71 | 0.31 | 584 | 311 | 191 | 90 | 86 | Explosive phase |
| 2009/04/10 | d | 286.4 | 4.3 | 260.6 | 25.8 | 14 | 4 | 116.33 | 0.94 | 531 | 258 | 148 | 370 | 222 | |
| 2009/05/05 | d | 342.1 | 17.4 | 269.4 | 72.7 | 38 | 32 | 463.50 | 3.75 | 606 | 333 | 51 | 351 | 85 | |
| 2009/05/09 | n | 337.6 | 16.9 | 261.6 | 76.0 | 88 | 65 | 454.20 | 3.68 | 750 | 477 | 162 | 281 | 138 | |
| 2009/05/18 | d | 295.4 | 5.4 | 266.5 | 28.9 | 50 | 37 | 141.45 | 1.15 | 624 | 351 | 233 | 231 | 155 | Effusive phase |
| 2009/06/06 | d | 292.9 | 5.0 | 275.2 | 17.7 | 30 | 17 | 89.18 | 0.72 | 668 | 395 | 209 | 244 | 248 | |
| 2009/06/12 | d | 323.9 | 7.6 | 271.8 | 52.1 | 46 | 37 | 305.27 | 2.47 | 733 | 459 | 156 | 268 | 132 | |
| 2009/07/08 | d | 311.5 | 6.7 | 280.0 | 31.5 | 31 | 24 | 179.64 | 1.46 | 610 | 337 | 139 | 269 | 135 | |
| 2009/08/09 | d | 278.1 | 2.1 | 270.5 | 7.6 | 14 | 7 | 34.21 | 0.28 | 738 | 465 | 219 | 36 | 23 | |
| 2009/08/25 | d | 271.1 | 1.8 | 265.2 | 5.9 | 3 | 0 | 25.13 | 0.20 | 579 | 306 | 279 | 162 | 177 | |
| 2009/09/07 | n | 284.0 | 2.9 | 268.0 | 16.0 | 44 | 17 | 74.22 | 0.60 | 617 | 344 | 225 | 183 | 200 | |
| 2009/09/23 | n | 268.9 | 2.9 | 253.1 | 15.8 | 66 | 48 | 61.75 | 0.50 | 472 | 199 | 153 | 365 | 288 | |
| 2009/09/26 | d | 285.3 | 5.5 | 260.2 | 25.1 | 49 | 31 | 112.34 | 0.91 | 578 | 305 | 200 | 348 | 467 | |
| 2009/11/01 | d | 265.9 | 3.3 | 252.5 | 13.4 | 61 | 44 | 51.41 | 0.42 | 637 | 364 | 197 | 74 | 43 | Post-eruption |
| 2009/11/13 | d | 266.4 | 3.5 | 246.2 | 20.2 | 51 | 26 | 74.89 | 0.61 | 616 | 343 | 174 | 109 | 67 | |
| 2009/11/20 | d | 265.2 | 4.0 | 248.1 | 17.1 | 62 | 51 | 63.75 | 0.52 | 479 | 206 | 147 | 317 | 256 | |
| 2009/12/10 | n | 287.8 | 4.4 | 264.3 | 23.5 | 79 | 66 | 108.86 | 0.88 | 539 | 266 | 113 | 111 | 43 | |
| 2009/12/13 | d | 282.3 | 4.9 | 260.8 | 21.5 | 68 | 59 | 94.69 | 0.77 | 512 | 239 | 110 | 343 | 253 | |
| 2009/12/31 | d | 275.9 | 4.3 | 256.0 | 19.9 | 53 | 40 | 82.43 | 0.67 | 673 | 400 | 196 | 122 | 102 | |

Once a volcano is identified as having increased thermal output, ASTER is automatically tasked and the volcano is targeted at the next available opportunity. This ASTER Urgent Request Protocol (URP) provides a limited number of emergency observations, typically at a much-improved temporal resolution and quicker turnaround with data processing in the United States rather than in Japan. The ASTER URP can speed the reception of the processed data by several days to a week (Duda et al., 2009a, 2009b).

ASTER has acquired over 330 individual scenes over Redoubt Volcano since June 2000. More than 180 of these images offer clear to partly

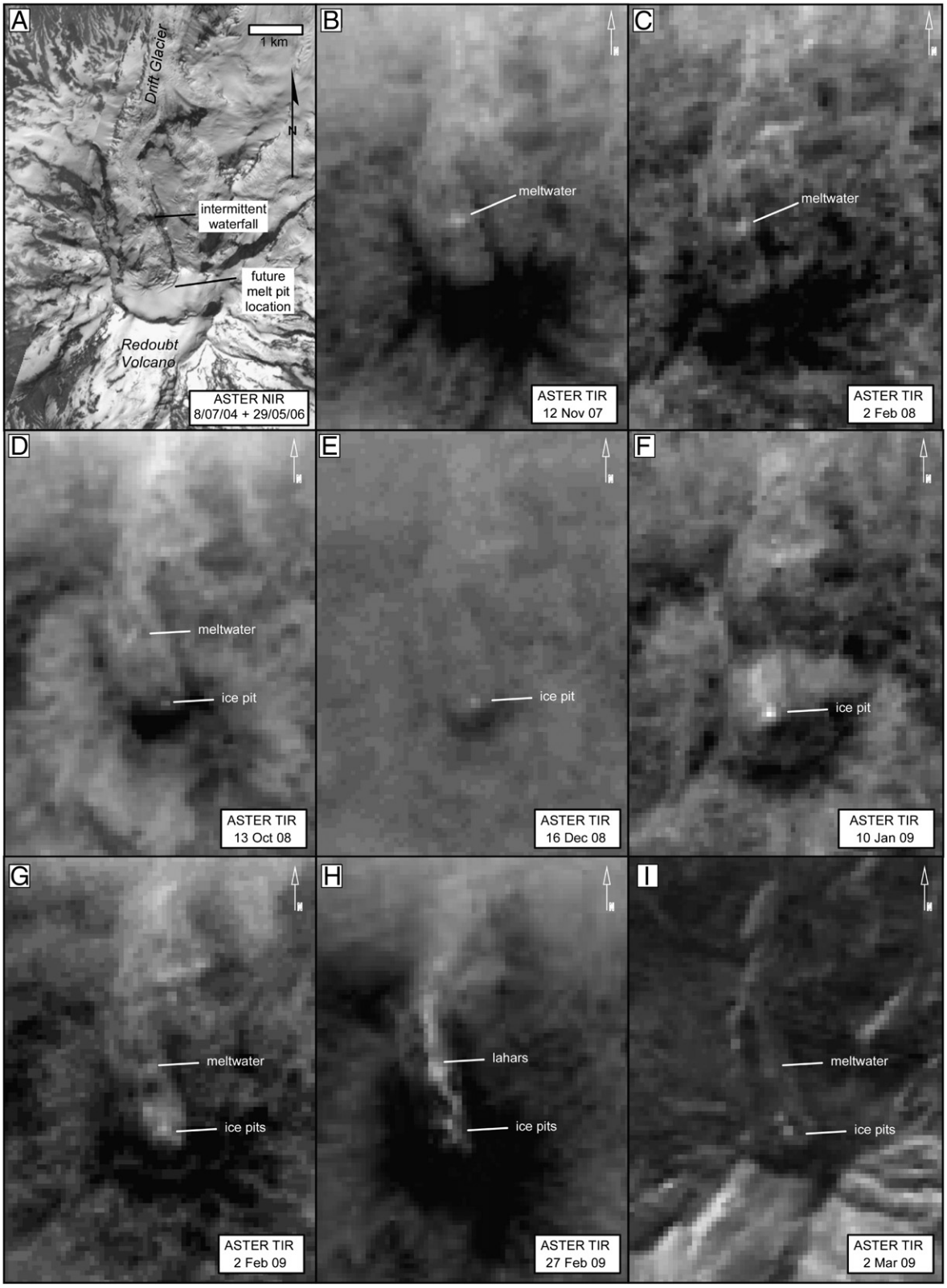


**Fig. 3.** (A) ASTER NIR image (band 3 N) showing thermal features on Redoubt Volcano before the 2008–2009 unrest. (B–I) Series of ASTER TIR band 11 images showing pre-eruption low-temperature thermal features in the summit crater and above BG meltwater at an intermittent waterfall half way down the Drift Glacier.

cloudy day and night views. In 2008 and 2009 ASTER data were acquired over Redoubt Volcano on 86 dates (Appendix 1). Of these 86 acquisition dates, 41% are cloud-free, 10% are partly cloudy such that Redoubt Volcano's summit area is only partly obscured, and the remaining data are completely cloudy and/or obscured by volcanic plume. About 55% of these acquisitions were acquired at night, between 07:40 and 08:40 UTC. Nighttime data are ideal for isolating the surface emitted radiance component from subtle thermal features because of increased thermal contrast. The ASTER Level-2 data products used include: AST09T atmospherically corrected at-surface TIR radiance (Thome et al., 1998) and AST08 surface kinetic temperature data (Gillespie et al., 1998).

*3.2.1.1. ASTER data analysis.* For each ASTER scene in 2008 and 2009 with a clear view of the Redoubt Volcano crater, a region was defined around the central part of the crater that contained any visible thermal anomalies relative the surrounding area in the AST08 kinetic temperature image. As an example, Fig. 2 shows the ASTER nighttime temperature image from 10 January 2009 showing a subtle thermal anomaly (a few bright pixels relative to surroundings). The smaller, inner area is the crater area evaluated for thermal anomalies. The larger area is the surrounding background (BG) area to which the crater area was compared. These areas were selected subjectively by visual inspection. In this scene, the average temperature of the BG area = 248.2 K (−25 °C); the temperature of hottest pixel in the thermal area = 260.8°K (−12.35 °C); the ΔT = 12.6°K (Fig. 2 and Table 2). Nighttime ASTER data are acquired for the Redoubt Volcano area around 11 pm local time. The use of nighttime TIR data minimizes, but does not completely eliminate, the effects of solar radiance absorbed during the day and re-radiated at night. There is still a component of surface emitted radiance that is not geothermal in origin as evidenced by the fact that non-thermal areas have sufficient temperature to emit TIR radiance at night. This non-geothermal emitted radiance is largely a function of solar heating during the previous day, which is a function of topography (elevation, slope, and aspect), land surface cover, and previous weather conditions. To isolate the geothermal component of the radiant emittance and heat flux from the crater area, a BG subtraction method was used. The average radiant emittance value (in $W*m^{-2}$) from a proximal, non-geothermal BG area was subtracted from the radiant emittance values from pixels in the thermal area, on a pixel-by-pixel basis, to derive the geothermal component of radiant emittance and geothermal heat flux. The assumption here is that the thermal

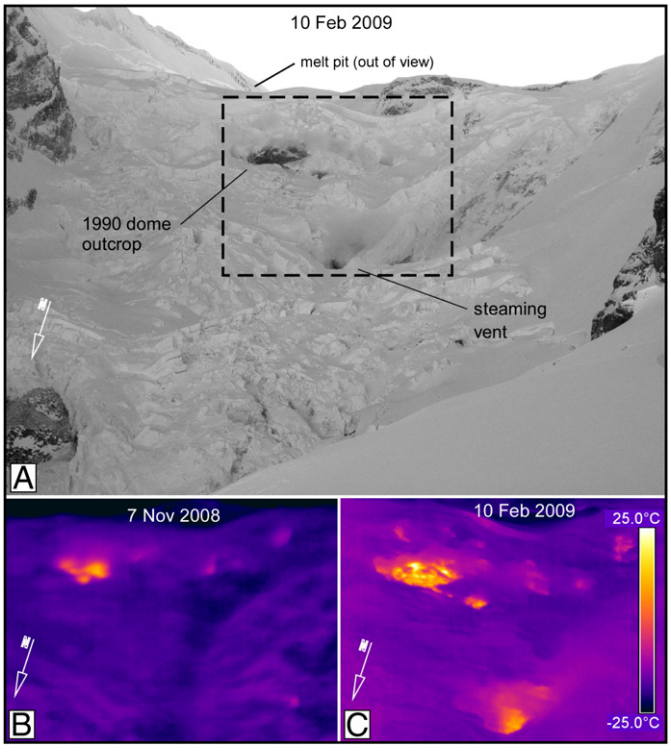


**Fig. 4.** (A) Oblique photograph showing dominant melt features of the summit crater area viewed from the north taken on 10 February 2009 with area imaged in B and C outlined by the dashed rectangle. (B) 7 November 2008 FLIR image showing melt pits slightly above BG. (C) 10 February 2009 of the same area showing larger warmer summit features.
Photo by Game McGimsey, USGS-AVO.

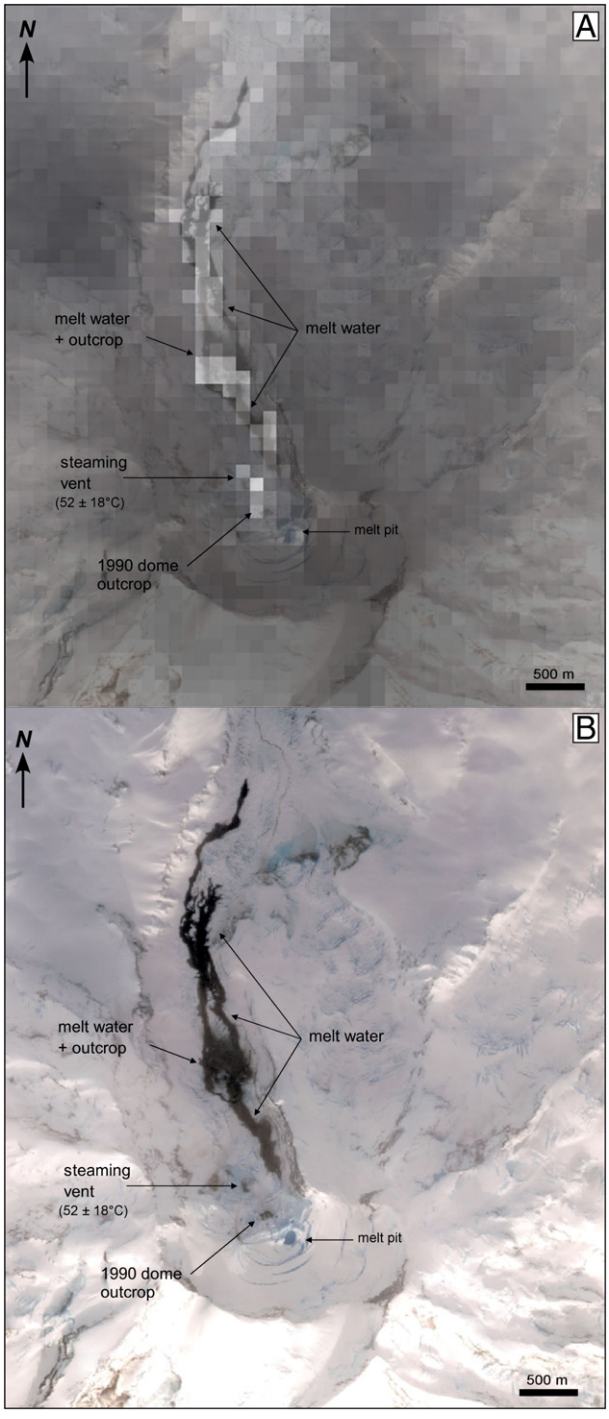


**Fig. 5.** (A) 27 February 2009, 21:52:59 UTC, QuickBird VNIR image showing details of melting of the summit ice features and new flowage deposits observed by ASTER TIR in B 12 h earlier. (B) 27 February 2009, 07:40:56 UTC, zoomed-in ASTER nighttime TIR image showing estimated sub-pixel temperatures for early outflow deposits and thermal features.
QuickBird Copyright 2009 Digital Globe, Inc.

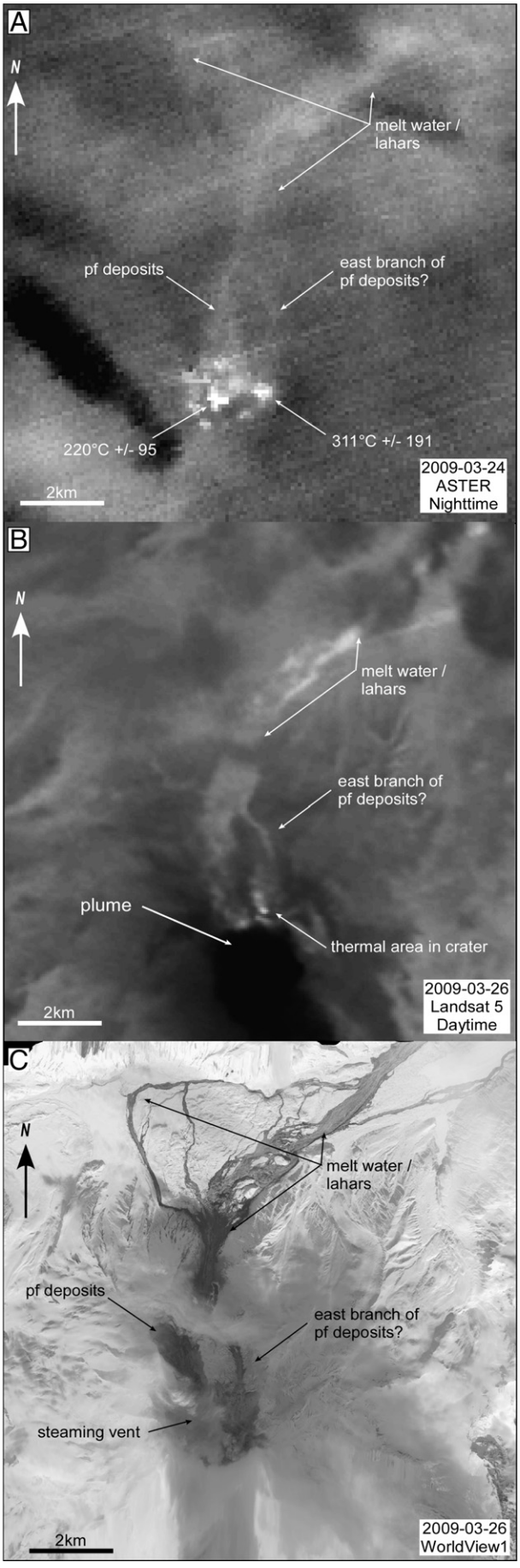


radiance emitted from the non-geothermal BG areas is almost entirely a function of how much solar radiance was absorbed in that area during the previous day, and that this value is very similar for the proximal thermal area. By choosing nearby non-geothermal BG areas with topographic and land surface cover characteristics that are as similar as possible to the geothermal area justifies this assumption, however, the presence of small unequally distributed clouds or plume material from crater area is a source of uncertainly. The BG subtraction method should also minimize variations related to seasonal changes. The total radiant emittance ($M_T$, in $W*m^{-2}$) from the crater area was derived on a pixel-by-pixel basis using the Stephan–Boltzmann equation ($M_T = \sigma\varepsilon T^4$), where $\sigma = 5.6704*10^{-8}$ ($W*m^{-2}*K^{-4}$) and T = the ASTER pixel temperatures (K). Emissivity ($\varepsilon$) for the area was assumed to be 0.97, which is the average for a mixture of andesite and ice from the ASTER spectral library (Baldridge et al., 2009). The geothermal component of the radiant emittance ($M_G$) was calculated by subtracting the BG radiant emittance ($M_{BG}$) from the total radiant emittance ($M_T$). The radiant geothermal heat flux ($\phi_G$, in MW) was attained by multiplying $M_G$ by the corresponding pixel area ($M_G$ * area of an ASTER 90-m pixel (8100 $m^2$)), and summed for various groups of pixels in the thermal area, including all the pixels with temperatures greater than the mean temperature of the BG area, >1, >2, >3, and >4 standard deviations above the mean temperature of the BG area, and for the single hottest pixel.

*3.2.1.2. ASTER sub-pixel temperature estimates.* ASTER 09T surface radiance data were used to model the sub-pixel temperature components for anomalously radiant pixels for dates with clear thermal anomalies, starting in December 2008 (Table 2). It is possible to estimate the characteristics of sub-pixel-scale thermal features using spatially and temporally coherent multi-channel TIR measurements. The simplest method for such thermal modeling, the two-component method, has been described by Dozier (1981), Rothery et al. (1988), and Harris et al. (1999). Such modeling assumes a two-temperature component system where there is a single hot target of a certain sub-pixel area, surrounded by a cooler BG that encompasses the rest of the pixel area. If one of the unknown parameters (either temperature or area, of target or BG) can be assumed or measured independently, then multi-channel TIR measurements can be used to estimate the remaining parameters. The wider the wavelength separation of the TIR measurements, the more unique the solution can be. In other words, TIR measurements in the 3–5 μm range (or in the 1–2.5 μm range for very hot targets) combined with the 8–12 μm range are ideal. With ASTER data, however, only the TIR data in the 8–12 μm region can be used because of questionable pixel-for-pixel spatial co-registration between ASTER's SWIR and TIR channels and the lack of SWIR data during this eruption of Redoubt Volcano. Theoretically, the 5 ASTER TIR channels should be capable of modeling sub-pixel thermal features with a sufficient ΔT between target and BG temperature, but there are larger uncertainties associated with using TIR channels so close together (i.e., all in the 8–12 μm range) (Vaughan et al., 2010).

*3.2.2. Landsat TM and ETM+*

Other TIR data sources used to fill in time gaps in the ASTER coverage include the Thematic Mapper (TM) instrument on Landsat 5 and the Enhanced Thematic Mapper Plus (ETM+) on Landsat 7. Normally the Landsat imagers acquire little, if any, data over Alaska during the winter months. However, the USGS Landsat team responded to the Redoubt Volcano unrest by acquiring both day and night Landsat 7 data and daytime Landsat 5 data beginning in February 2009 and continuing through

**Fig. 6.** (A) 24 March 2009, 07:35:00 UTC, partly cloudy ASTER nighttime TIR view showing hot features in the summit crater and warm lahar deposits nearly 4 h after explosive event 6. (B) 26 March 2009, 21:07:11 UTC, Landsat 5 daytime TIR image. (C) 26 March 2009, 21:51:02 UTC, WorldView-1 image showing recent deposits about 4.5 h after event 8.
WorldView-1 image Copyright 2009 Digital Globe, Inc.

most of the year. These special acquisitions combined with the large image swath overlap at high latitudes provided 7–9 Landsat views of the Redoubt Volcano area each month of the 2009 eruption. Our database consists of 72 Landsat 7, 59 day and 13 night, and 38 Landsat 5 day only images obtained between 2008 and 2009, of which about 50 provided clear to partly cloudy views of the summit (Appendix 1).

*3.2.3. Commercial sensors*

AVO also had access to a variety of high-resolution commercial satellite VNIR images and synthetic aperture radar (SAR) data throughout the initial unrest and eruption. QuickBird, WorldView-1, and IKONOS provided 75 daytime panchromatic and false color images from late 2008 through 2009 (Appendix 1). These wide-pointing spaceborne systems provided frequent views of the summit at 0.5–4-m spatial resolutions. The combination of sensors provided daily views throughout much of the early stage of the eruption. Besides providing detailed views used to refine our observations as described in Section 4, these data were very useful for tracking small features within the glaciers before the eruption (Bleick et al., 2013) as well as dome structures during effusion (Bull et al., 2013). Furthermore, orthorectified versions of the commercial images sometimes helped correct geo-coding uncertainties in the ASTER nighttime data. Unfortunately, a combination of cloudy weather and thick plumes typically obscured the majority of syn-eruption views of the summit crater and domes.

Synthetic Aperture Radar (SAR) systems are able to image through thick clouds and plumes. Radarsat-2 is a commercial Canadian SAR satellite with multiple swath widths, resolutions, and polarization modes. Two Radarsat-2 SAR backscatter images provided unobstructed views of the summit during the eruption. The data were collected using its highest resolution 1-m Spotlight mode using either horizontal (HH) or vertical (VV) send/receive polarization.

## 4. Results

*4.1. Pre-eruption unrest*

Section 4.1 summarizes the thermal features observed in high-resolution TIR observations of Redoubt Volcano during the months before the eruption. While this section also includes a small subset of high-resolution visible satellite images and oblique photos for context, see Bleick et al. (2013) for detailed observations and measurements of all pre-eruption surface changes in the summit area and down the Drift Glacier.

Early hints of possible new unrest at Redoubt Volcano began with several reports of plumes extending from the summit in 2006 and 2007. While AVO often receives reports of plumes at Cook Inlet volcanoes when meteorological conditions are conducive to cloud formation, each new report triggers an internal review of satellite and seismic data for any new anomalies. A particularly well-defined plume was observed and photographed on both 24 and 25 February 2007. An ASTER URP daytime image acquired on 6 March 2007 shows a small dark area in the ice field near the location of 1990 dome in the summit crater area as well as a dark area down glacier where a large waterfall appeared in early 2009. While no thermal anomalies were observed in an ASTER URP nighttime TIR image from 10 March 2007, two ASTER TIR images from 22 February and 3 March may detect very weak TIR anomalies of the water fall area. These potential anomalies are barely above the TIR image noise, so they are uncertain. Observations made during August 2007 flights noted that the 1990 dome area appeared to be visible in recent crevasses just below the surface of the ice.

Clear ASTER nighttime TIR data from 2000 to 2007 show that the permanently ice-covered summit, crater and the upper edifice remained at ambient BG temperatures with no obvious thermal anomalies detected

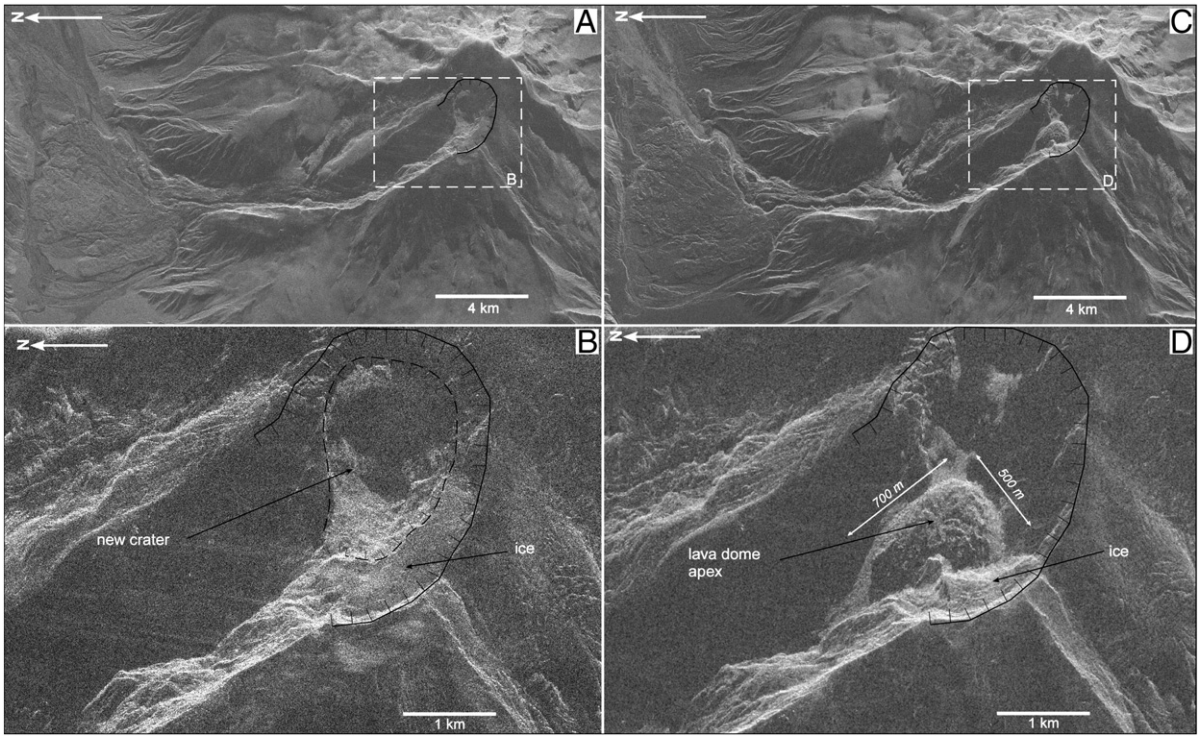


**Fig. 7.** (A) Overview of 27 March 2009 16:24:29 UTC Radasat-2 SAR HH-polarized backscatter view of Redoubt Volcano summit to the north end of the Drift Glacier piedmont lobe. (B) Enlarged view, outlined by white rectangle in figure A, of summit area showing a large blast crater and crater ice field remnant. (C) Overview of 20 April 2009 16:24:32 Radarsat-2 SAR VV-polarized backscatter view of Redoubt Volcano summit to the north end of the more eroded Drift Glacier piedmont lobe. (D) Enlarged view, outlined by white rectangle in figure C, of summit area showing an enlarged crater area and the final lava dome filling much of the crater. Surface features extend radially from the apex of the dome.

until late 2007. On 12 November 2007, ASTER nighttime TIR (Fig. 3B) shows one of the first clear indications of a thermal anomaly below summit crater half way down the Drift Glacier. This is approximately the location of an ice pit that formed over a persistent waterfall (Fig. 4A), first observed during the fall of 2008 (Bleick et al., 2013). This anomaly is still very low temperature, but somewhat clearer than the apparent anomalies detected near the same location in early 2007.

Changes in fumarole activity and reports of hydrogen sulfide ($H_2S$) odors were first noted at Redoubt Volcano late in the summer of 2008. Persistent areas of steaming through pits and crevasses in the ice-filled summit crater (Fig. 4) developed during Fall 2008 until late January 2009. Weak ASTER TIR thermal anomalies began to appear at the summit crater on 13 October and 12 December 2008 (Fig. 3D, E, and Table 2). Fall 2008 also marked the beginning of above-background gas emissions (Werner et al., 2013), volcanic tremor (Buurman et al., 2013), and steaming from a 50-m-wide pit (Fig. 4) on upper Drift Glacier (see Bleick et al., 2013; Werner et al., 2013; Bull and Buurman, 2013).

Airborne FLIR data acquired on 7 November 2008 detected maximum temperatures of 20 °C over a small steaming melt pit that formed in the ice over the 1990 dome (Fig. 4B and Table 1). Given a −19 °C BG at 2350 m a.s.l. elevation, the feature was 39 °C above the cold BG. Severe in-flight turbulence prevented direct FLIR views down into the pit. The maximum FLIR temperature is likely much less than the actual surface temperature at the bottom of the pit due to the poor viewing conditions combined with the low ambient temperature. The FLIR temperature of a waterfall at the lower northeast edge of the Drift piedmont glacier was 6.2 °C in a −5 °C BG at about 1200 m elevation. Water temperatures recorded during sampling about 1.5 km downstream of the falls were 1.5 °C in −10 °C ambient.

From January through mid-March 2009, growing summit thermal anomalies and intermittent water outflow events down the north flank of the volcano in the large Drift Glacier valley were the dominant features detected in high resolution TIR data (Fig. 3F–I and Table 2). On 23 January, watery mudflows began to sporadically discharge from below the summit fumaroles down the upper Drift Glacier and into the Drift River (Bleick et al., 2013; Waythomas et al., 2013) as the level of seismicity and gas emissions rose significantly.

A clear ASTER nighttime TIR image from 2 February shows larger areas of warm summit features and open water and new flowage deposits down the upper Drift Glacier and the upper Drift River valley (Fig. 3G). A FLIR survey taken eight days later, on 10 February (Fig. 4C), shows warmer and larger summit features compared with FLIR views on 20 November (Fig. 4B and Table 1). The maximum FLIR temperature of the pit above the 1990 dome increased to 28.6 °C in a −17 °C BG (45 °C above BG). The outflow at the base of the Drift Glacier was a chilly −1 °C in a −15 °C BG (Table 1).

Unfrozen water and new lahar deposits extending northward down the length of the Drift Glacier and eastward down the Drift River valley appear as obvious thermal features in a 27 February 2009 ASTER nighttime TIR (Figs. 3H and 5A). The details provided by a high-resolution daytime QuickBird image taken about 12 h after the ASTER TIR aid in the interpretation of the variations in thermal features seen in an enlarged view of the ASTER TIR image (Fig. 5B). The ASTER pixel-integrated temperatures (PIT) from the hottest few pixels range from −8 °C to −10 °C with BG temperatures ranging from −18 °C to −25 °C (Table 2). Sub-pixel temperature components were estimated using ASTER TIR surface radiance data and assuming a 2-temperature component system (Vaughan et al., 2010). The hottest pixel in the crater area from 27 February 2009 was calculated to contain a high-temperature component at 52 ± 18 °C covering an area of 276 ± 1100 $m^2$ (Table 2). The large uncertainties in the estimated temperature and area of the hot component are due to a combination of assumptions about emissivity, BG temperature, the number of temperature components, and uncorrected atmospheric effects (Vaughan et al., 2010).

The final pre-eruption ASTER image from 2 March 2009 shows two discrete summit thermal features with now obvious outflow deposits (Fig. 3I). Landsat 5 and 7 acquired the only high-resolution TIR views of Redoubt Volcano during the three weeks before the first large explosive events on 23 March. Landsat 7 nighttime TIR data from 15 March 2009 detects several warm areas from summit crater down Drift Glacier (Appendix 1). Outflow and recent lahar deposits are visible in Drift River valley. A WorldView-1 image from 15 March 2009 at 21:12:39 UTC shows a thick white plume partially obscuring fresh dark deposits from a 15 March phreatic event (Schaefer, 2012 and Bull and Buurman, 2013) that occurred 7 min before the satellite overpass. A Landsat 7 daytime view on 18 March 2009 shows steaming from the open summit ice pit, but weak TIR summit thermal features appear to be similar to the 15 March nighttime view.

### 4.2. Explosive phase

After several months of pre-eruption unrest, the phreatic explosion on 15 March was followed one week later by a series of at least 19

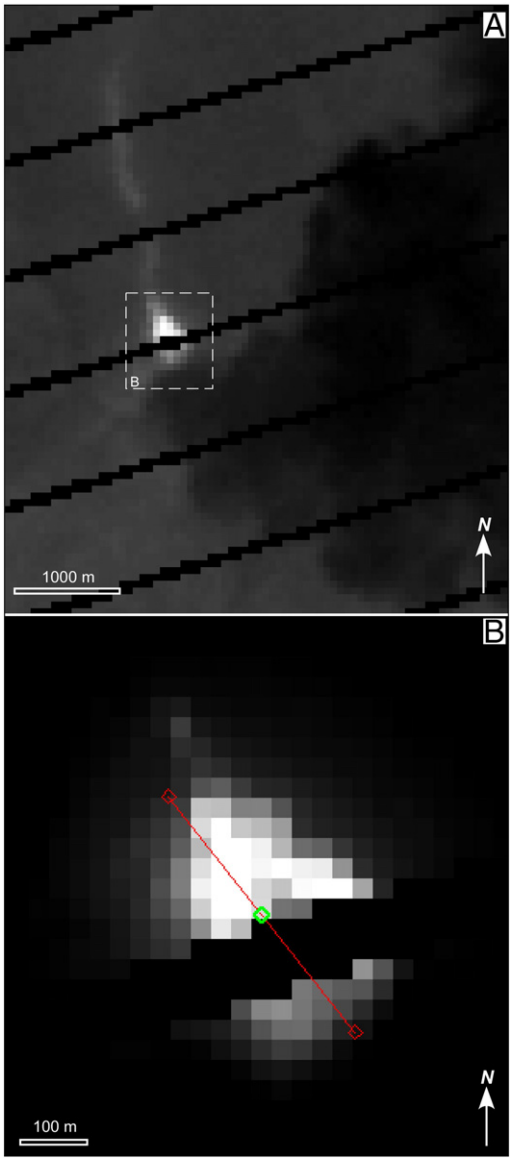


**Fig. 8.** 31 March 2009, 7:12:46 UTC Landsat 7 nighttime TIR and SWIR images revealing the lava dome extending from beneath an opaque plume. (A) 60-m TIR image showing the dome, lahars, and dark plume. Dashed box shows area of B. (B) 30-m SWIR showing the hottest parts of the dome. The diagonal line along the crest of the dome is 450 m.

magmatic explosive events (23 March–4 April UTC, Appendix 1) that produced high-altitude ash clouds and large lahars (Bull and Buurman, 2013). At least two lava domes were extruded and destroyed between 23 March and 4 April (see Bull et al., 2013).

Explosive events 1–6 produced a variety of ash clouds, pyroclastic flows, and lahars. The first high-resolution TIR was an ASTER nighttime image (Fig. 6A) acquired less than 4 h after explosive event 6 (24 March 2009 at 03:41 UTC). Event 6 produced a small pyroclastic flow and cloud that flowed down Drift Glacier, as well as lahars on the East shoulder and in the main Drift gorge drainage. While the ASTER TIR view is partly cloudy, the clouds are thin enough to see thermal radiance in the crater and from running water and fresh deposits down the valley. The ASTER TIR image also shows a narrow band of warm deposits on the east flank where a pyroclastic flow melted the ice and created a debris flow in the east gorge that flowed into main Drift Glacier gorge (Fig. 6A).

There are also several warm areas in crater including two distinct high temperature areas about 1 km apart. ASTER 90 m PITs of these features range from −12 to −14 °C with BG temperatures that range from −16 to −19 °C. The estimated sub-pixel temperature component of hottest 2 pixels was 311 ± 191 and 220 ± 95 °C, comprising areas of 90 ± 86 and 93 ± 64 $m^2$, respectively (Fig. 6A and Table 2). The highest estimated sub-pixel temperatures, up to 311 °C, are located in the center of the crater (eastern most hot spot) suggesting a lava dome. A second smaller area of high temperatures, up to 220 °C, lies in the western part of the crater. Although ASTER TIR sub-pixel temperature calculations have large uncertainties, the multiple sources of error (emissivity, BG temperature, and in this case, thin cloud cover) might offset, yielding essentially realistic hot target temperature values. While the plume in Landsat 5 and WorldView-1 images from 26 March mostly obscures the summit area, the images show the continued tephra and lahar deposition down the Drift River valley caused by explosive events 7 and 8 (Fig. 6B and C).

Explosive events 9 through event 18 occurred 27–28 March (Schaefer, 2012; Bull and Buurman, 2013, and Appendix 1). High resolution Radarsat-2 provided much needed views of the developing crater through the clouds and plume during this period. A SAR backscatter image, acquired 27 March at 16:24:29 UTC about 8 h after event 11, shows a large, nearly 1-km-wide blast crater where the permanent snow and ice used to be and gullies eroded into the Drift Glacier by lahars (Fig. 7A and B). Due to the high cost of these data relative to other options, only one more RadarSat-2 summit view was acquired during this event on 20 April 2009 (Fig. 7C and D).

Early on 31 March, a little over two days after event 18 (Schaefer, 2012), Landsat 7 nighttime TIR and SWIR bands observed a lava dome extending northward from beneath a thick plume (Fig. 8A, B, and Appendix 1). The lava dome measured on the SWIR image was at least 450 × 285 m. Landsat TIR data also shows the recent lahar and tephra deposits on the upper Drift Glacier above BG temperatures. FLIR data collected 10.5 h after the Landsat 7 image briefly detected the base of

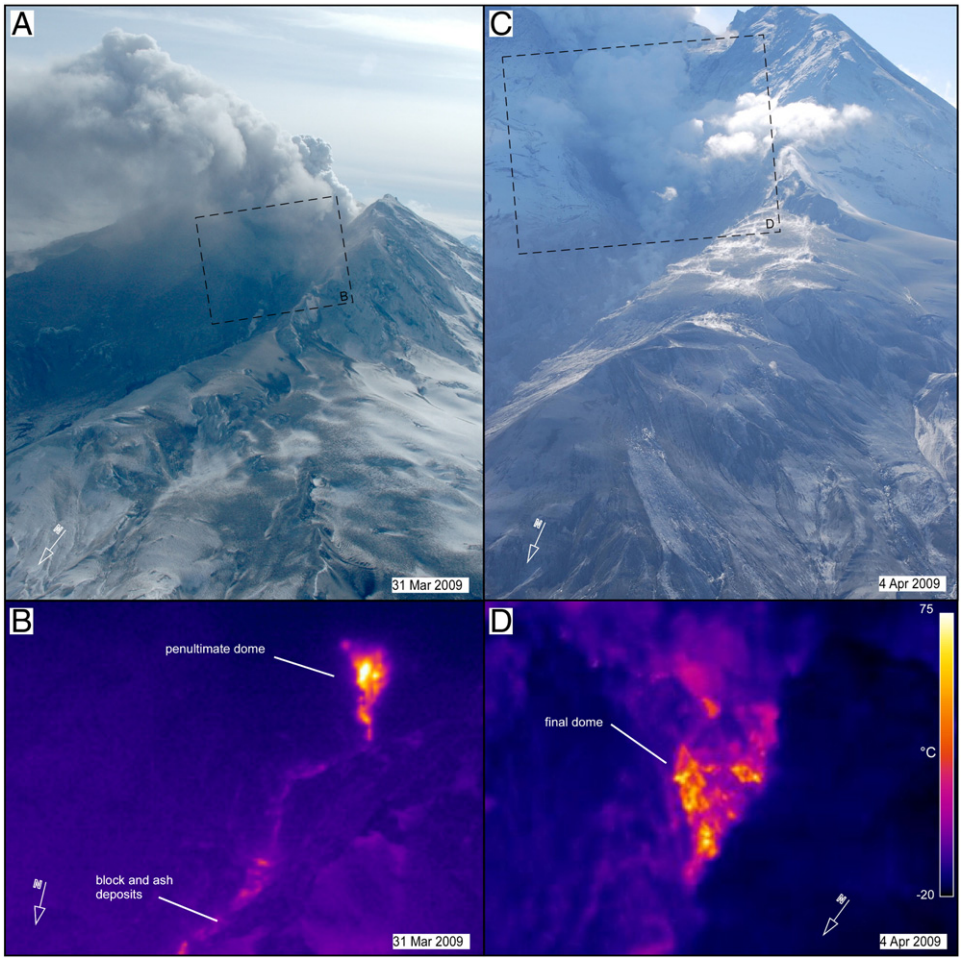


**Fig. 9.** Oblique photographs and FLIR views of Redoubt Volcano acquired four days apart, before and after the final explosive "event #19". (A, B) 31 March 2009, 17:44 UTC (10.5 h after the Landsat nighttime TIR in Fig. 8). Photo (A) and FLIR (B) views from 7.3 km NW of the active dome. Dashed box shows approximate area of B. The FLIR view reveals the north base of penultimate lava dome and hot block and ash deposits below the dome. A thick gas and ash plume obscures the upper portions of the dome (photo by Game McGimsey). (C, D) 04 April 2009, 21:45 UTC (same time as WorldView image in Fig. 10). Photo (C) and FLIR (D) views taken from 6 km NW of the active dome. The FLIR view reveals the earliest stages of the final lava dome beneath a thick shroud gas and ash emissions.

the north lobe of the lava dome beneath the thick continuous plume (Fig. 9A, B). Maximum FLIR temperatures were 127 °C in a BG of −20 °C (Table 1). The actual temperatures were likely much higher behind the fume and ash obscuring the dome.

### 4.3. Effusive phase

Event 19 marked the end of the explosive phase and beginning of the effusive phase of the 2009 eruption (Schaefer, 2012). Based on repeated dome volume measurements, the effusive phase continued through approximately 1 July 2009 (Bull et al., 2013, and Diefenbach et al., 2013). The first FLIR survey of the effusive phase was conducted less than 4 h after event 19 (Fig. 9C, D, and Appendix 1 and Table 1). Though extremely thick fume obscured most of the crater, a few views showing a high temperature area near the vent location suggest that the final lava dome of the 2009 eruption began to extrude almost immediately after the final explosion (Fig. 9C, D). A maximum FLIR temperature of 112 °C (2.6-m pixels), observed near the base of the crater, was likely an underestimate due to the thick fume obscuring hot features within the crater (Table 1). The apparently blocky surface had a minimum average temperature of about 33 °C. WorldView-1 data acquired 4 h after the FLIR survey show the thick plume over the crater, new pyroclastic flow deposits on the upper flanks, and dark lahar flow deposits extending down Drift Glacier and Drift River valley (Fig. 10).

After 4 April, poor weather and a thick continuous plume obscured most of the crater until an ASTER nighttime TIR image captured a partial view on 10 April (Fig. 11A). Since this is a daytime scene, there are some solar heating effects seen on south facing slopes (e.g., south side of crater). Again, two distinct hot areas appear within the crater and are separated by about 1 km with the eastern most hot spot coinciding with the crater at the top of the new dome. The highest sub-pixel temperatures measured for the two hottest pixels in the crater area were 258 ± 148 °C and 238 ± 123 °C (Fig. 11A, Table 2). In WorldView-1 images from both 4 and 5 April (Fig. 10), both areas appear to be sources of plumes with the largest plume coming from the highest temperature area.

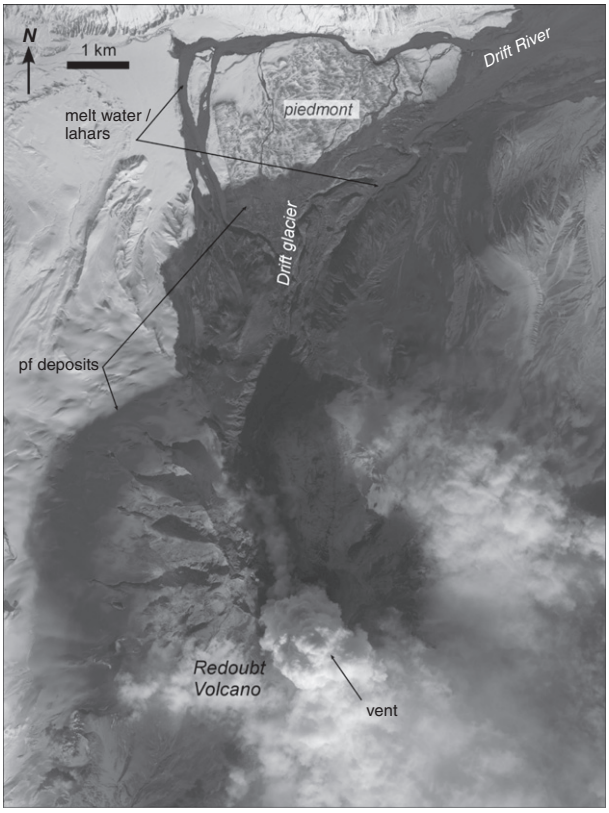


**Fig. 10.** 4 April 2009 21:41:18 UTC WorldView-1 panchromatic image, acquired less than 8 h after event 19, showing dark deposits from large lahars and pyroclastic flows. WorldView-1 Copyright 2009 Digital Globe, Inc.

Landsat 7 nighttime TIR data from early on April 16 show a faint view of the dome beneath the thick plume and cloud cover (Fig. 11B). Approximately fourteen hours after the Landsat 7 view, a 16 April FLIR survey and photos observed active rockfalls tumbling down the block north tongue of the dome (Fig. 12A). The maximum FLIR temperature was 430 °C integrated over 1.6 m pixels (Table 1). The average dome surface temperatures ranged from 65 °C on the south side of the dome to over 118 °C along the active north side (Fig. 12A). The hottest areas are linear zones of either freshly exposed lava and/or fractures that stretch from the top central portion of the dome to the outer edges of the talus. The approximate dome dimensions from several oblique FLIR views were 600 m N–S, 420 m E–W, and 158 m above the visible base of the crater floor.

A 20 April high-resolution Radarsat-2 view shows a large dome filling much of the summit crater (Fig. 7C and D). The 1-m backscatter image suggests that blocky lava covers the entire dome surface with linear fractures or ridges that extend out radially from the apex of the dome. The dome dimensions measured from the terrain-corrected backscatter image was about 700 m long by 500 m wide (Fig. 7D). The image also shows pronounced erosion of the upper Drift Glacier below the dome and along the lower part of the glacier in the Drift River valley (Fig. 7C).

An ash-rich plume blowing north off the dome on 30 April prevented direct views of the north side of the dome. The FLIR survey, viewing the dome from south, east, and west (Fig. 13A and B), imaged hot blocky lava covering the dome surface with individual fractures reaching FLIR (1.8-m pixels) maximum temperatures up to 314 °C at the dome apex vent (Table 1). The FLIR views also provided early measurements of the dome dimensions from the south end. The length from the southern edge over the apex to the steep, north-slope transition was about 492 m; to the northern end of the lava was about 760 m; the east–west width was 450 m; and the vertical height from crater base to the dome top is estimated to be 180 m based on slope distance. The hottest spots visible in this image lie on the north side of the very top of the dome, radial streaks or fractures on the south side, and western edge as it cascades down the steep northern slope.

Landsat ETM+ nighttime TIR and SWIR data from 2 May provide the first relatively clear views of the final dome (Figs. 11C and 14A). While the geocorrected 60-m ETM+ TIR image from 2 May shows the generalized shape and structure of the dome surface (Fig. 11), the 30-m SWIR view highlights the hot apex vent and the lower blocky facies (Fig. 14A). The scaled images suggest dome axis lengths of about 770 m long by 460 m wide across the apex (Fig. 14A). ASTER nighttime TIR data from 9 May show the continued growth of the dome providing dome axis lengths of about 825 m long by 470 m wide (Fig. 14B). The larger 90-m pixels likely cause an overestimate of the dimensions.

Starting 8 May 2009, FLIR images (Figs. 12B and 15A) begin to show a vertical segregation of both temperature and texture between a cooler upper facies and a hotter lower blocky unit at the base of the dome (Bull et al., 2013). The lower apparent surface temperature of the upper facies may indicate the development of a cool surface crust on the dome. The lower TIR temperature might also indicate a lower density or emissivity caused by a difference in lava surface texture such as higher lava vesicularity or a coating of fine material. The apex of the dome and the talus at the margins and northern toe of the dome also have higher temperatures than the upper facies. The maximum FLIR temperature, measured near the north base of the dome, was 273 °C with average temperatures of 21 °C for the upper facies and 75 °C for

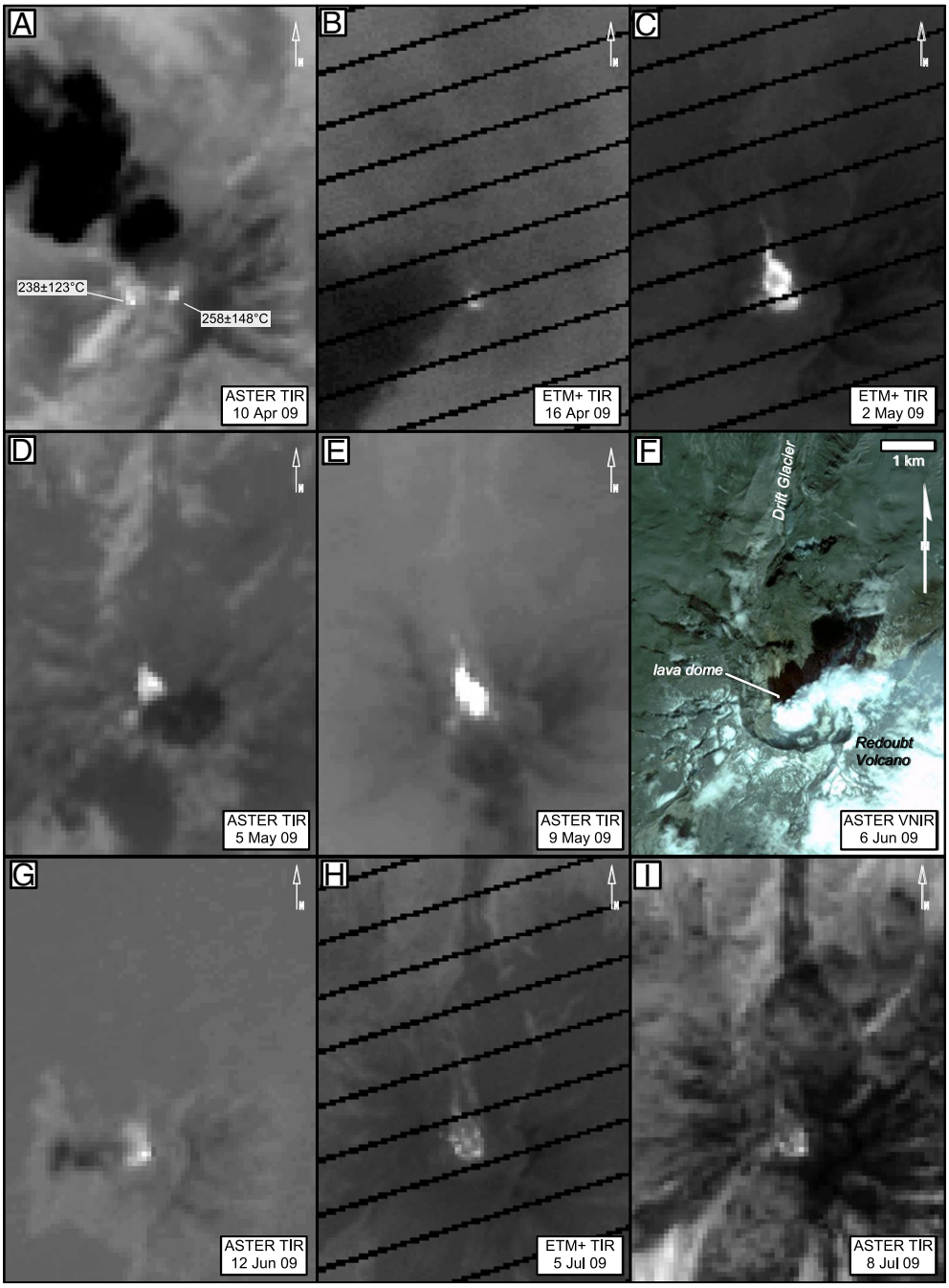


**Fig. 11.** Series of high-resolution satellite TIR images from ASTER (90-m) and Landsat ETM + (60-m), from 10 April 2009 to 08 July 2009, spanning most of the effusive phase of the 2009 Redoubt Volcano eruption. The selected images demonstrate the variations in scene quality, temperature distributions, and active dome areas. The highest temperatures in the 9 May ASTER (E) correspond with a period of higher effusion rate. The Landsat ETM + TIR images have black diagonal scan lines. Image 13 F is a higher resolution visible-near-infrared (15-m) daytime ASTER. All images are displayed at the same scale as F.

the lower facies (Figs. 12B and Table 1). Approximate dome dimensions measured from both FLIR and simultaneous TIR satellite images were about 800 m long, 450 m wide, and 187 m tall. The 9 May ASTER nighttime TIR had a maximum 90-m PIT of 65 °C located along the blocky lower facies on the north side of the dome (Figs. 11E, 14B, and Table 2). The estimated sub-pixel temperature for a 280 $m^2$ area was 477 ± 162 °C (Table 2).

16 May FLIR images and photographs show that the rubble-covered upper facies has begun to dominate the north side of the dome surface (Figs. 12C and 14A). The areas of the blocky margins of the dome are slightly thinner and cooler compared to the 8 May FLIR. The apex of the dome and the radial fractures around the blocky margin are also relatively hot. The maximum FLIR (1.3-m pixels) temperature was 345 °C at the apex vent with average temperatures for the upper facies at 31 °C and the blocky lower facies at 45 °C (Table 1). Approximate dome dimensions measured from both FLIR and a satellite image from a 17 May WorldView-1 image (Fig. 16B) were about 900 m long, 475 m wide, and 210 m tall.

FLIR views from 9 June show that a much cooler, rubbly, upper facies (average FLIR temperature now 0 °C) appears to have covered most of the lower blocky facies on the north side of the dome (Figs. 12D and 13C–D). A thin layer of blocky material continues to be exposed at the base of the north toe of the dome. A hot blocky surface (average FLIR temperature of about 33 °C) now seems to cover most of the dome to the south of the apex (Fig. 13C and D). The highest temperatures were detected at the apex of the dome with a maximum FLIR

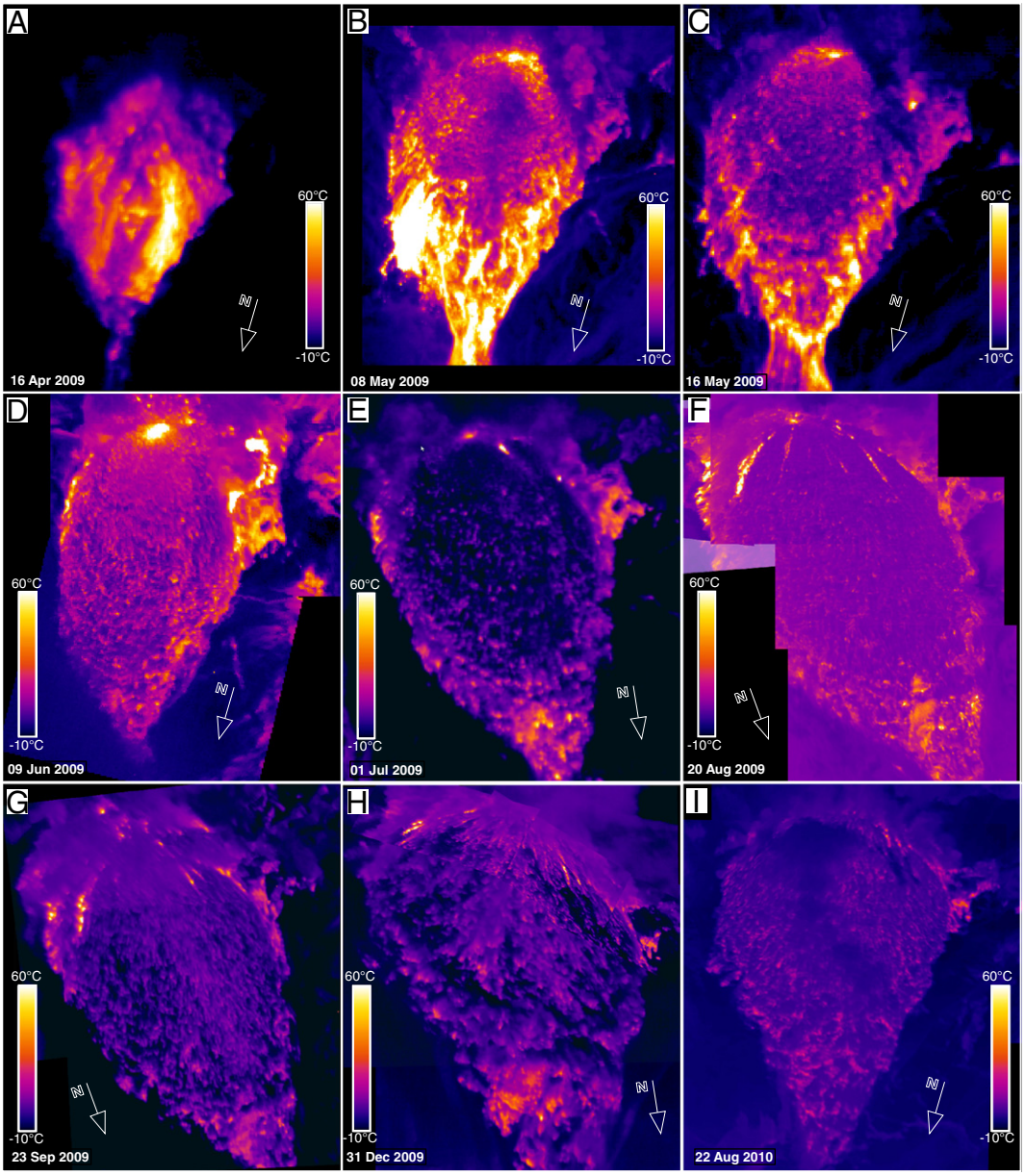


**Fig. 12.** FLIR views documenting the growth and cooling of the final Redoubt Volcano lava dome viewed from the north to northeast from 16 April 2009 through 22 August 2010. For easier comparison, the temperature range for each image is linearly stretched to a scale of −10 to 60 °C.

temperature >260 °C (likely much higher since sensor gain was exceeded). Hot rockfalls continue to slough onto the talus cone below the toe of the lava dome. The contact between the cooler, rubbly, upper facies and the warmer, blocky facies appears to strike approximately E–W, dipping about 60° north from apex down to the base of the dome (Fig. 13C and D). Nighttime ASTER TIR data from 12 June suggest that the dome surface was cooler than early May (Fig. 11G). The 90-m ASTER TIR maximum PIT is 50 °C on the SE flank of the dome (Table 2).

The dome growth and the eruption likely ceased about 1 July 2009 based on dome volume measurements (Diefenbach et al., 2013). FLIR data from 1 July (Fig. 12E) show the warmest features at the apex vent area and the southern blocky areas (maximum temperature >260 °C with an average surface of 20.6 °C). The cooler, rubbly, upper facies covers most of the dome's north side with average surface temperatures of 6 °C. The blocky margin is generally smaller on the north flank and cooler than in previous images (Fig. 12E). Approximate dome dimensions measured from both FLIR and simultaneous satellite images were about 950 m long×465 m wide. Satellite TIR data from the same week show continued cooling of the dome surface compared to May and June 2009 (Fig. 11H and I). An ASTER daytime TIR image measured a maximum PIT of 35 °C.

### 4.4. Post-eruption

Satellite and airborne high resolution TIR data show continued, gradual cooling of the dome surface during the 13 months following the eruption (Tables 1 and 2, Figs. 17 and 18). FLIR data collected on 20 August 2009 show that fractures seen in oblique images (Bull et al., 2013) are visible as linear, relatively hotter regions on the FLIR images (Fig. 12F). The survey also provides glimpses of the southern and eastern sides of the dome showing additional radial fractures that begin at the dome apex. The south half of the dome continues to expose a relatively hot, blocky surface with an area southwest of the apex vent

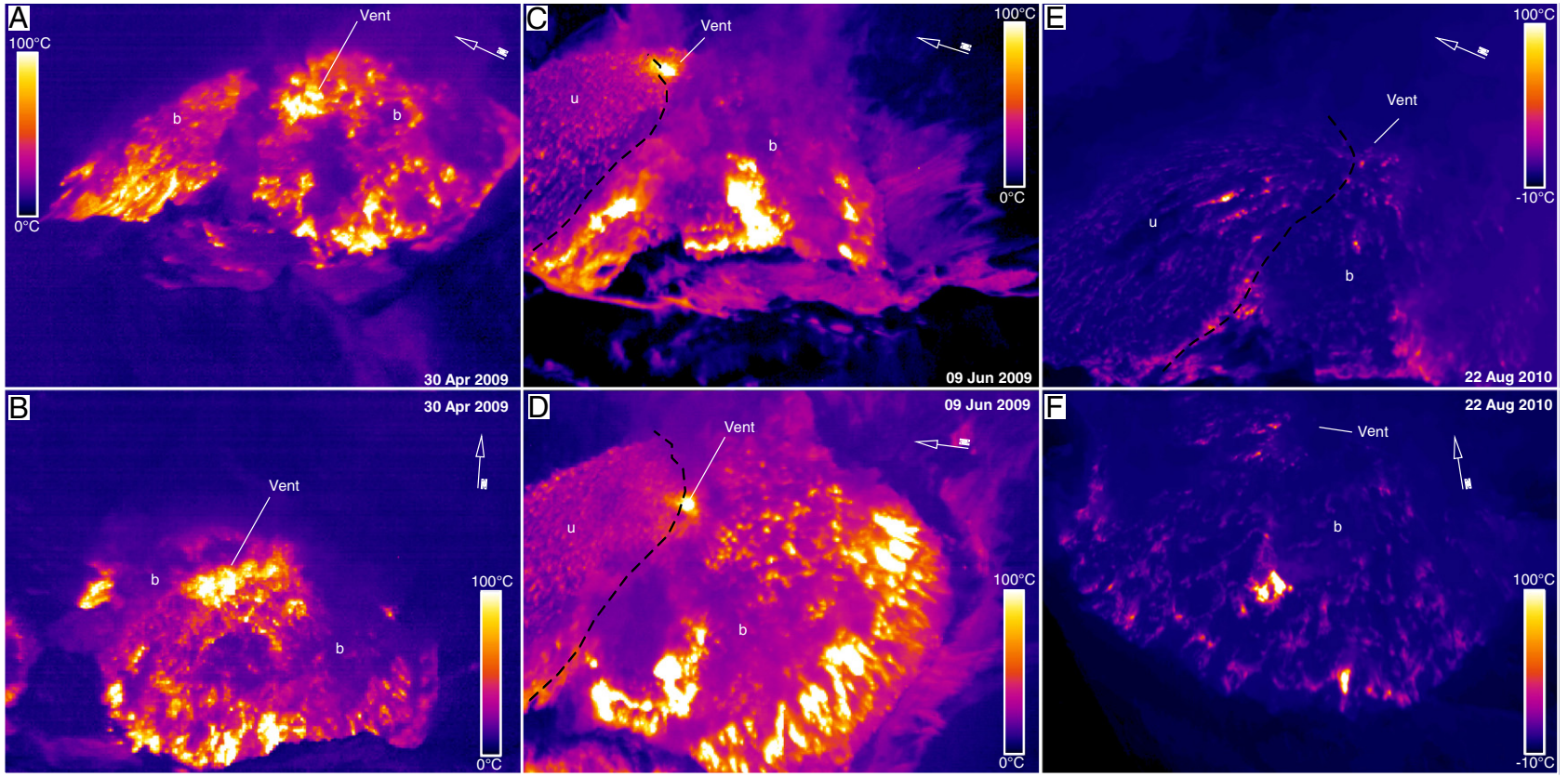


**Fig. 13.** FLIR views from different angles and distances of the S and SW flanks of the lava dome showing the dominant surface morphologies and vent area. (A, B) 30 April 2009 views suggest the entire dome surface is uniformly large massive blocks; $T_{max} = 260$ °C. (C) 09 June 2009 show the more fragmented upper scoriaceous facies north of the vent, left of the dashed line, while remaining blocky south of the vent. $T_{max} > 260$ °C. (D). Higher altitude view showing more of the south side of the dome and the two primary dome textural facies. $T_{max}$ for the vent was 160 °C. (E, F) 22 August 2010 views showing a few small high temperature fractures and fumaroles ($T_{max} > 150$ °C) sparsely scattered across a much cooler dome surface more than one year after the end of the eruption.

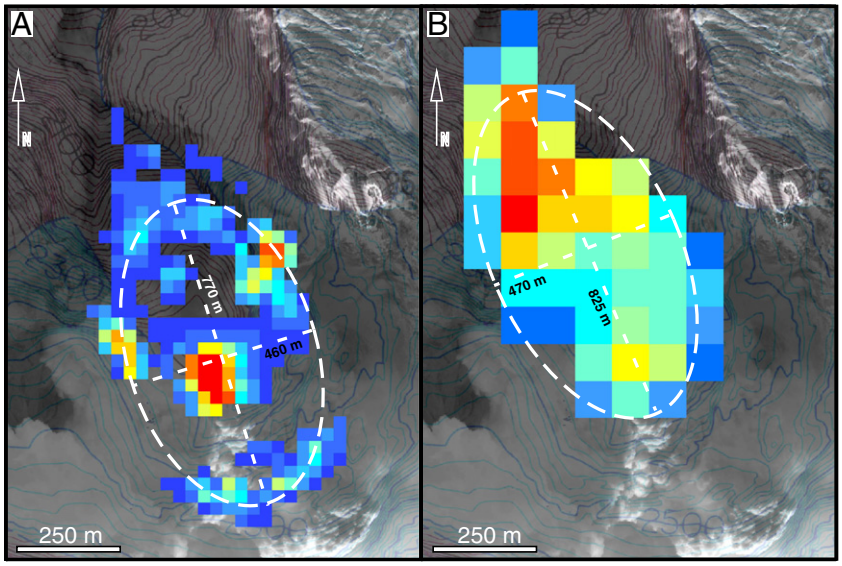


**Fig. 14.** (A) 2 May 2009 07:40 UTC Landsat 7 ETM+ nighttime SWIR over 16 May QuickBird showing dome dimensions measured from the hottest pixels. The 30 m SWIR pixels only show the hottest areas on the dome. Portions of the dome south of the apex were obscured by a thick plume. (B) 9 May 2009 07:47:09 UTC ASTER nighttime TIR. The 90 m TIR pixels are sensitive to much lower temperatures, thus appearing to be a more complete view of the dome surface. Both images show the distribution of hot areas at the apex and base of the dome. Note the slight apparent increase in dome area from 2 May to 9 May. Comparison with dimensions from higher resolution images in Fig. 16 suggest that dimensions using the larger satellite TIR pixels can create errors of at least 100 m in the SWIR and more than 200 m in the ASTER TIR.

yielding the highest maximum FLIR temperature of 363 °C (Fig. 19A, B, and Table 1). While this temperature is higher than dome $T_{max}$ values from May through July, it is mainly a result of flying the aerial surveys closer to the dome. The shorter imaging distance and better viewing conditions yield smaller pixel sizes and less attenuation by volcanic fume than the earlier dome surveys. The maximum apex vent temperature was about 130 °C. A nighttime Landsat ETM+ 60 m TIR and 30 m SWIR bands, acquired roughly 36 h later on 22 August 2009, show several of the high temperature areas measured by the ~1.5-m FLIR images on 20 August (Fig. 19C and D). The locations of the hottest areas on the south side of the dome and apex appear to be the same as observed in the June FLIR data (Fig. 13C and D). Clear nighttime ASTER TIR data from 7 September show that while the dome surface continues to cool, the persistent thermal areas maintain maximum sub-pixel temperatures of 343 ± 225 °C (Table 2). FLIR surveys on 23 September and 31 December 2009 document the continuing cooling of the dome surface with several high temperature areas remaining at the apex vent, lower dome margins, and blocky south half (Fig. 12G, H, and Table 1).

High-resolution satellite and FLIR TIR data show that most of the high temperature features observed during Fall 2009 persisted up to one year later (Figs. 17 and 18). Comparison of FLIR images collected on 09 June 2009 and 22 August 2010 (compare Fig. 13C, D to E, F) shows several geothermal areas persisting in the same locations. The average surface temperature had cooled to −5 °C with maximum temperatures along some of the fractures and fumaroles exceeding 260 °C. From Fall 2009 through 22 August 2010 (Fig. 12I), average surface temperatures of the dome measured by several FLIR surveys and ASTER TIR maximum PIT stabilize to only a few degrees above BG temperatures (Tables 1, 2, Fig. 17A and B). Hot fumaroles along the blocky margins and south side persisted throughout late 2009 with maximum FLIR temperatures >250 °C and estimated maximum ASTER sub-pixel average 240 ± 109 °C (Tables 1, 2, Fig. 18A and B).

## 5. Discussion

### 5.1. Sub-pixel temperatures from satellite TIR

The 1-km resolution near-real time AVHRR and MODIS data did not detect thermal unrest at Redoubt Volcano until several days after the start of the 2009 eruption (Webley et al., 2013). However, high-resolution ASTER TIR data were able to detect subtle anomalies in crater surface temperatures several months before the first large seismic swarms and explosions. Fig. 17B shows the number of crater pixels that were >3 and >4 standard deviations (SD) above the BG mean AST08 surface kinetic temperature, with anomalous values appearing by November 2008. This appears to be a useful metric for detecting precursory thermal activity. Whereas time-series analyses of 90-m PIT for ASTER TIR are relatively straightforward, these data only show clear thermal anomalies once the eruption has begun. Using the five ASTER TIR channels to estimate higher sub-pixel temperatures of features within a 90-m pixel are subject to large errors, but are nevertheless also useful for measuring pre-eruption temperatures that are indicative of anomalous warming in the crater and often in reasonable agreement with FLIR temperature data. In this study, ASTER TIR surface radiance (AST09T) data were used to estimate the highest sub-pixel temperatures from the hottest (most radiant pixels) in each scene by assuming a BG temperature based on the AST08 pixel temperatures of proximal non-thermal pixels (Figs. 17 and 18). However, independent knowledge of the range of expected hot target temperatures acquired from FLIR measurements was critical. For example, knowing that 24 March 2009 is the first time one would expect to see silicate lava eruption temperatures at the surface allows constraints on range of possible temperatures. Before the initial eruptive event (22 March 2009), there were anomalous thermal features in and around the crater area, but no magmatic temperatures should be expected at these times. So the range of expected temperatures could be limited to <100 °C.

As soon as ASTER TIR anomalies began to appear above melt pits in the summit ice cap during Fall 2008, temperatures where high enough to begin to model the sub pixel temperatures at Redoubt Volcano. Fig. 18B plots the estimated sub-pixel maximum temperatures, along with AST08 PIT for each of the hottest pixels in each scene from October 2008 through December 2009. While the pre-eruption AST08 PIT values from these relatively small features within the 90-m pixels averaged −12 ± 3.5 °C, the sub-pixel temperature estimates for the hottest features within the melt pits averaged 75 ± 35 °C (Table 2). Within error, this estimate compares fairly well with November 2008 and February 2009 FLIR maximum temperatures at the melt pits, measured through thick fume, of 39 to 46 °C (ΔT) above BG (Figs. 4 and 18A, Table 1).

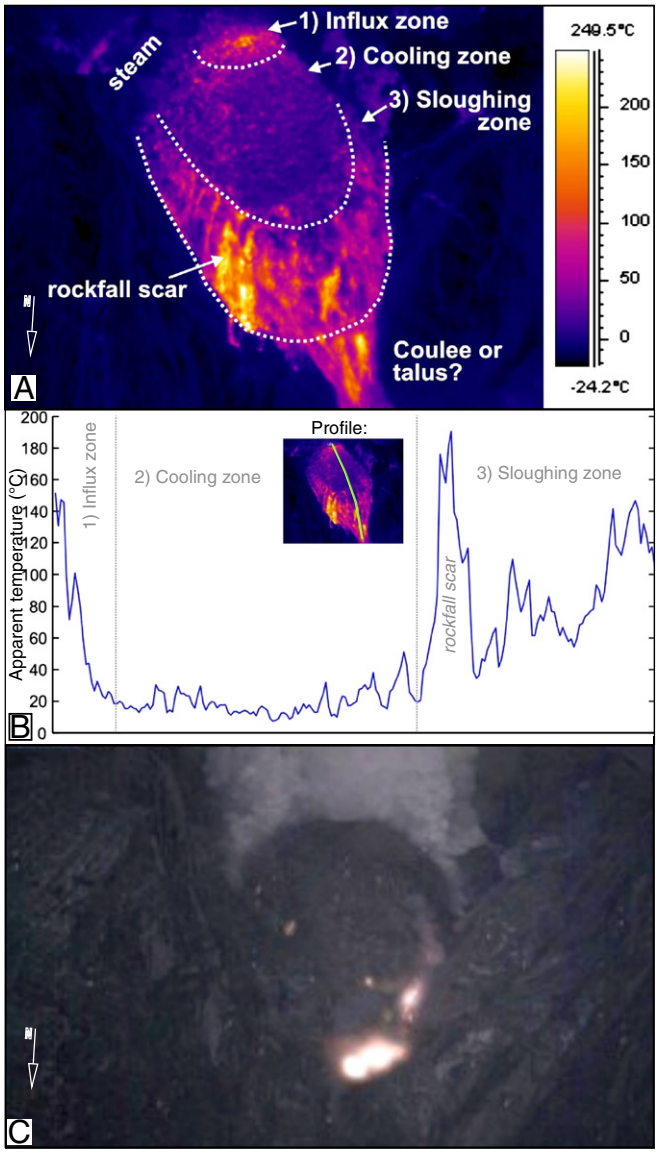


**Fig. 15.** (A) 8 May FLIR view from the north outlining dome thermal structure. (B) Temperature profile from the apex to the northern toe of the lava dome. (C) Composite of co-registered nightly webcam images (from 11 km north), showing all rockfalls that expose the incandescent dome interior captured between May 1 and 14.

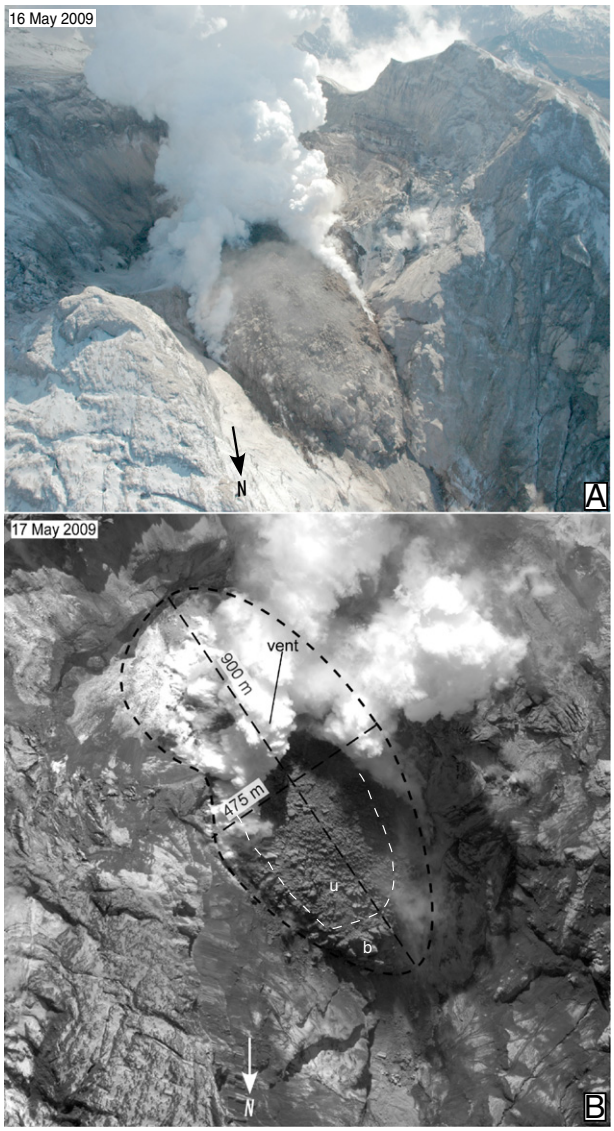


**Fig. 16.** (A) 16 May 2009 22:00 UTC oblique aerial view of the lava dome from the northeast acquired a few seconds before the 16 May FLIR view in Fig. 12C. (photo by Game McGimsey). (B) 17 May 2009 21:32:49 UTC WordView-1 satellite image showing full extent of the dome from the confined lakes on the southeast side of the dome to blocky toe of the lava extending down the north side The letters u and b mark the lower/southern blocky [b] surface and the later upper [u] rubbly dome surface. The satellite mage is rotated with North toward the bottom to approximate the view in A.
WorldView-1 Copyright 2009 Digital Globe, Inc.

Both AST08 PIT and sub-pixel temperatures rise substantially during the explosive and effusive phases of the eruption (images 24 March 2009 to 8 July 2009; Figs. 17 and 18, Table 2). With new lava at the surface, the average AST08 PIT temperature during this period increased to 33 ± 28 °C while the average maximum sub-pixel temperature increased to 375 ± 74 °C. The highest ASTER TIR temperatures of the eruption were detected on 5 and 9 May 2009. Buurman et al. (2013) note a marked increase in the rate of total earthquakes per hour dominated by repeating events that often accompany high dome extrusion rates. These higher temperatures reflect an increase in the lava extrusion rate suggested by both the dome volume measurements (Diefenbach et al., 2013) and the seismic data (Buurman et al., 2013).

A comparison of the 8–9 May FLIR and ASTER TIR data, described in Section 4.2, shows a discrepancy in the maximum derived temperatures. While the 9 May maximum AST08 PIT of 65 °C is in good agreement with the 8 May FLIR average surface temperature of 75 °C, the ASTER sub-pixel estimate (477 ± 162 °C) is about 200 °C higher than the FLIR $T_{max}$ (273 °C). One might expect the 1–2 m FLIR pixels to detect temperatures at least as high as the sub-pixel estimates from 90-m ASTER TIR pixels. It is not clear whether this discrepancy reflects issues with the sub-pixel model assumptions (most likely) or simply differences in the dome surface, local atmosphere and viewing conditions between the two datasets.

Post-eruption satellite and airborne TIR data after 8 July document locally elevated dome surface temperatures throughout the remainder of 2009 (Fig. 17A, B, and Tables 1 and 2). The average maximum AST08 PIT during this period was 2.4 ± 8.5 °C, 14 °C higher than the PIT of the pre-eruption TIR features. The PIT is within error of FLIR mean surface temperatures of 6.5 ± 6 °C during the same time. The average ASTER sub-pixel temperature of the hottest dome features post-eruption was 312 ± 82 °C; 237 °C warmer than the pre-eruption features though approximately 53 °C cooler than the effusive phase average. This is in good agreement with FLIR data acquired during this period with a 299 °C mean $T_{max}$ (309 °C above $BG_{mean}$); about 257 °C above the pre-eruption FLIR $T_{max}$. Most of the high temperatures occur along several persistent

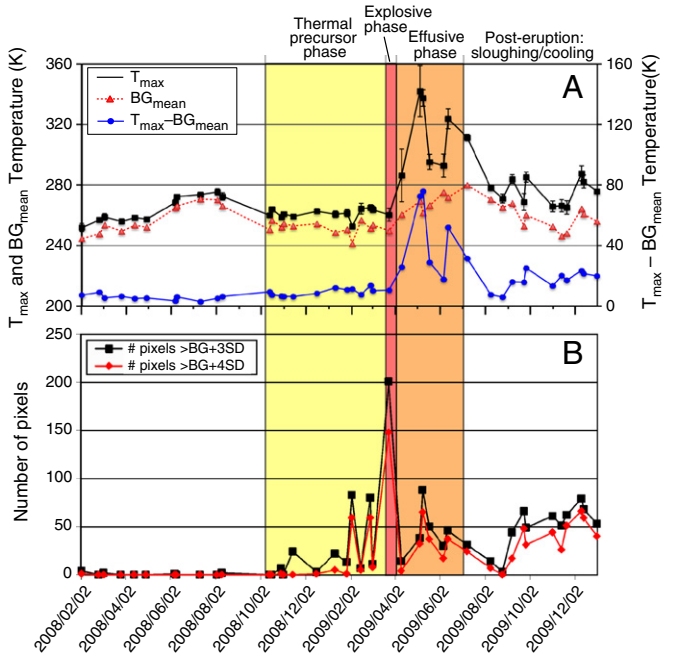


**Fig. 17.** Temperatures and areas from February 2008 — December 2009 ASTER TIR data: (A) Time series plot of AST08 pixel-integrated temperature (K) of single hottest pixel $T_{max}$ (squares) and mean background $BG_{mean}$ (triangles) on the left axis and $T_{max} - BG_{mean}$ (circles) on the right axis on each date for both day and night TIR. (B) Time series plot of the number of 90-m pixels >3 (squares) and >4 (diamonds) standard deviations (SD) above the mean BG temperature.

hot fractures and outcrops with vigorous emissions. The hot features also led to weak thermal anomalies in the 1 km pixels of AVHRR and MODIS data from late 2009 through early 2010 (Webley et al., 2013).

### 5.2. FLIR insights into dome structure

Beginning on 4 April 2009, oblique photographs and FLIR images (Fig. 9C and D) show that the surface of final dome was mostly

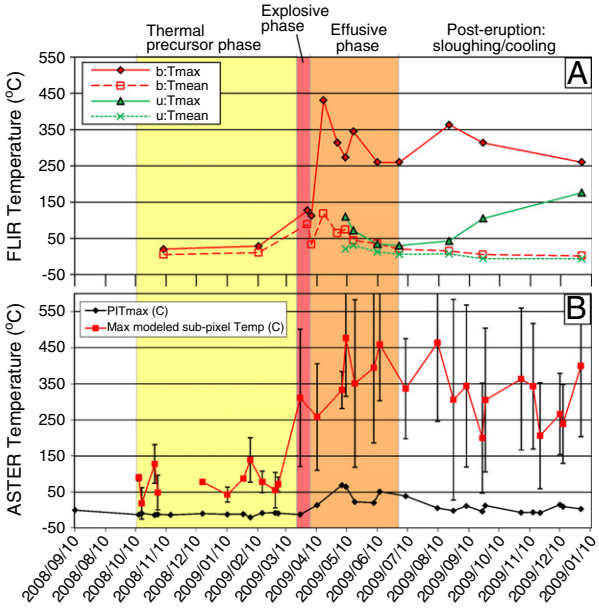


**Fig. 18.** Time series plot of FLIR and ASTER observations spanning August 2008–December 2009: (A) FLIR $T_{max}$ and $T_{mean}$ for the lower/southern blocky [b] surface and the later upper [u] rubbly dome surface. (B) AST08 temperature [diamonds] and modeled ASTER sub-pixel maximum temperature [squares] for single hottest pixel from clear ASTER TIR data.

comprised of hot, large blocks of lava with much of the dome forming a coulee down the gorge of above the upper Drift Glacier (Bull et al., 2013). The upper surface of the dome began to appear more rubbly and cooler in early May. FLIR images after early May suggest a new structure to the lava dome north of the vent consisting of three thermal zones, going from (1) hot to (2) cool to (3) hot again (Fig. 15A). Generally, these zones may be divided into three separate processes:

*Influx zone*: a circular high temperature region at the very top of the dome, which is presumably situated directly over the conduit. The region has an outer warm aureole, which is about 150 m wide, and a hotter inner core about 40 m wide. This region presumably is where the magma rises out of the conduit and begins exogenous lateral flow.
*Cooling zone*: as the lava spreads out radially from the influx zone, the surface cools significantly. Because the top of the dome has fairly shallow slopes, this region is immune to frequent small collapses, and the surface thermal gradient remains intact. Bull et al. (2013) identified this zone the scoriaceous, 55–66% vesicularity, "upper facies" that likely began to extrude around 1–3 May. This less dense, higher vesicularity surface would also cool more quickly than the denser blocks below.
*Sloughing zone*: the margins of the dome are inherently steeper than the top, and prone to frequent small rockfalls that expose the hotter core of the dome. Also, the northward portion of the dome is emplaced on a steeper underlying slope, increasing the instability along this margin. Bull et al. (2013) identify this zone as the "blocky facies" comprised of tightly spaced blocks with lower, 32 to 39%, vesicularity than the upper facies. This facies represents the early, blocky lava phase that preceded the May scoriaceous facies. FLIR images of the southern half of the dome suggest that the upper facies only flowed toward the north while the blocky facies continued to expand endogenously south of the conduit.

A simple thermal profile shows the three-zone structure in another manner (Fig. 15B). The influx zone appears to have an almost exponential decay in temperatures, while the cooling zone temperatures fall within a relatively narrow range. The sloughing zone temperatures are again elevated, with discrete peaks corresponding to individual rockfall scars. In addition to differences in age and activity of the various flow surfaces along this transect, the different textures, densities, and emissivity of the lava facies along transect will also influence the FLIR temperature profile.

The temperature distributions suggest that rockfalls were limited to the sloughing zone, and this is shown by nightly webcam views as well. At night, rockfalls on the dome are visible due to incandescence in the scar. Using Matlab (see Patrick et al., 2010), a composite was made of all the nighttime webcam images between 1 May and 14 May (excluding 4–7 May, in which the webcam zoom was set differently). This composite image (Fig. 15C) shows the brightest values at a given location in the image throughout the composite timespan. It shows that incandescent rockfalls were limited to the sloughing zone (with one large event visible in the coulee or talus region).

The sloughing zone is distinct to the naked eye as well, due to the different blocky surface texture (Fig. 20). On the low slopes of the cooling zones, rubbly scoria remains on the surface and no doubt aids in insulating the interior. On the steeper margins of the sloughing zones, loose material has fallen away, exposing the hotter, massive interior.

#### 5.2.4. Implications

FLIR images and oblique photographs from June 2009 and later suggest that the rubbly, scoriaceous surface observed and sampled on the dome north of the apex vent does not continue to the surface the dome south of the vent (Fig. 13C and D). The steeply north dipping contact between the upper facies rubble and the blocky lower facies

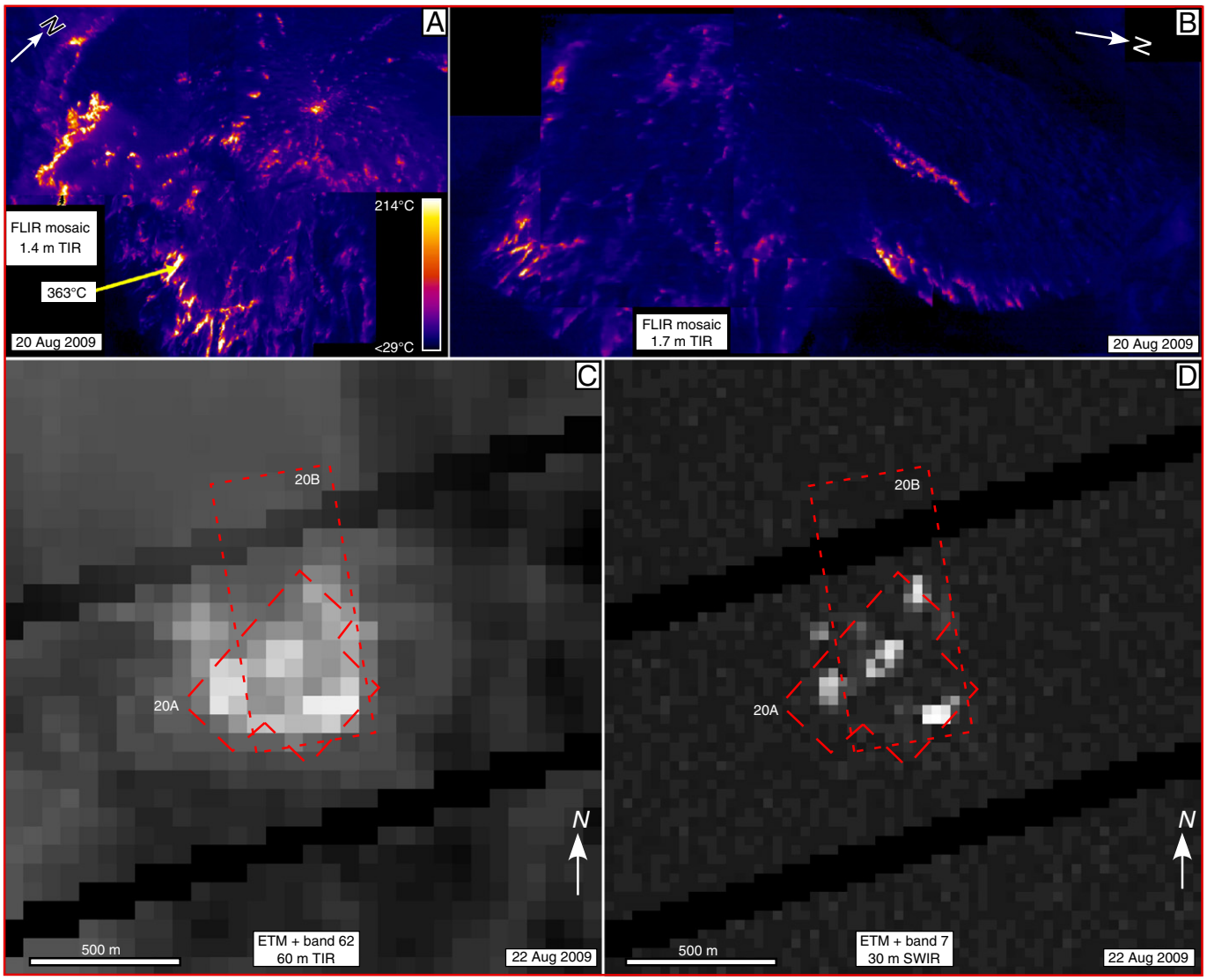


**Fig. 19.** A comparison of 20 August 2009, 18:45 UTC FLIR mosaics (A and B) to 22 August 2009, 07:12:40 UTC Landsat ETM + nighttime TIR (C) and SWIR (D) images demonstrates how the resolution differences between satellite and airborne TIR data might influence interpretations of cooling dome features . (A) FLIR view from the southeast shows discrete small, hot fractures are distributed within a relatively cool dome surface. Approximate area shown as the dashed "T-shaped" polygon on the Landsat images. (B) FLIR view from the east showing much of the length of the dome. Approximate area shown as the dashed rectangle on the Landsat images. (C) Landsat ETM + 60-m TIR of the crater and dome shows broad areas of warming as the small fractures integrate across the large 60 m pixels. (C) Landsat ETM + 30-m SWIR view of the same area as B. The SWIR's higher resolution and sensitivity to higher temperatures help the brightest Landsat pixels better correspond to the hottest areas in the FLIR views.

along with the gradually thinning exposure of the lower facies on the north side through May and June suggests that the upper facies exogenously extruded onto and over the lower blocky facies during the period of highest extrusion rates (Diefenbach et al., 2013; Bull et al., 2013), increased seismicity (Buurman et al., 2013) and an increase in $SO_2$ flux (Lopez et al., 2013; Werner et al., 2013). The segregated thermal structure implies that the scoriaceous upper facies flowed as a single coherent flow unit onto the north lobe of the dome as the south half of the dome slowly expanded endogenously. FLIR data showed hot linear radial fractures extending out from the apex vent beginning in June as effusion rates, based on dome volume measurements (Diefenbach et al., 2013), began to decrease. The appearance of the hot cracks and continued elongation of the rubbly upper facies through most of May indicates change to effusion from the apex. While the steep slope and east–west buttressing might have directed the outflow toward the north, it appears that most of the dome growth in late May through June was upward and toward the south (see Bull et al., 2013; Diefenbach et al., 2013). Webcam sequences showing surface material moving away from the vent at the top of the dome consistent with 'exogenous' emplacement of the upper facies (Bull et al., 2013). The temperature of the influx zone would be a more direct indicator of effusive vigor, as opposed to the temperatures of the sloughing zone, which is at best an indirect gauge of this parameter. The ASTER TIR data described in Section 5.1 appear to detect this period of higher effusion as a time of increased heat flux (Figs. 17 and 18).

Recent uses of thermal cameras for monitoring active domes around the world allow a comparison to Redoubt Volcano and provide insights on dome behavior in general. Like Redoubt Volcano, other domes imaged with thermal cameras show broad areas of remarkably low surface temperatures, often near ambient. The Mount St. Helens 2004–2007 dome (Schneider et al., 2009), as well as Bezymianny (Carter et al., 2007), Soufriere Hills (Young et al., 2007) and Santiaguito (Harris et al., 2002; Harris et al., 2003; Sahetapy-Engel and Harris, 2009) domes had much of their surface area at temperatures <100 °C during active

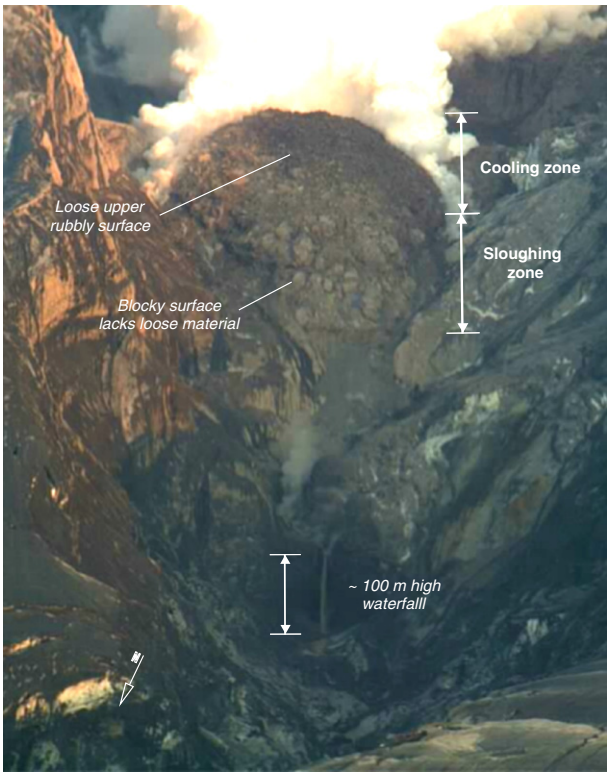


**Fig. 20.** 14 May 2009, 22:00 UTC webcam view detailing upper and lower dome surface textures.

periods. At Mount St. Helens, Bezymianny and Soufriere Hills, significant portions of the dome surface were composed of loose rubble or gouge, which appears to effectively insulate the solid, hotter interior.

Like the final lava dome of the 2009 eruption of Redoubt Volcano, localized regions of conspicuously high temperatures interrupt these broad areas of cool surface temperatures. These anomalously high temperature regions correspond to several features, including (1) degassing vents, (2) sloughing zones where rubble or other surface material falls off, (3) cracks (Mount St. Helens, Soufriere Hills, and Bezymianny) and (4) exposed lava extrusion (Redoubt Volcano, Santiaguito, and Mount St. Helens). First, hot degassing vents were observed along the margins of the Redoubt Volcano dome, and hot spots atop Santiaguito's dome mark the sites of active gas and ash emission. Second, sloughing of material from the dome surfaces exposes hot interior material, as has been observed at Redoubt Volcano, Mount St. Helens, and Soufriere Hills. Third, fracturing is ubiquitous on domes, and can indicate areas of instability as well as regions of shearing or differential movement (Mount St. Helens, Schneider et al., 2009; Bezymianny, Carter et al., 2007), or even endogenous growth (Soufriere Hills, Young et al., 2007). Fourth, discrete areas of high temperatures can represent areas of active extrusion on the surface. At Redoubt Volcano, the hot annulus is thought to be situated above the zone of lava upwelling, and at Mount St. Helens hot areas depicted the successive emergence of several spines (Schneider et al., 2009). These observations on fractures and areas of extrusion provide a picture of dome segmentation and can provide insight on the subsurface structure of the dome and conduit. For instance, thermal data were the basis for the model of shallow conduit structure at Santiaguito (Sahetapy-Engel and Harris, 2009). Taken together, these examples reinforce that thermal imagery provides a view of the structure and behavior of active domes with a clarity that is not possible with visual imagery.

### 5.3. Dome dimensions and volumes using satellite and FLIR images

Early in the effusive phase of the eruption of the final 2009 lava dome, the dome dimensions were estimated from scaled FLIR and satellite images within a few hours of acquisition (see Section 5.2). Ball and Pinkerton (2006) and Spampinato et al. (2011) detail the many complications from variations in atmosphere, surface properties, and viewing geometry that arise when using oblique FLIR to measure temperatures and dimensions. Though given the hazards presented by erupting, potentially explosive volcanoes, oblique FLIR views from distances of 1 to 8 km or satellite views from 700 to 900 km above are the only practical options for acquiring repeated TIR views. While individual FLIR pixel sizes can be well constrained for a known distance, the pixel size in an oblique view varies from smaller in the foreground to larger in the background. Calculating the detailed observation geometry from a number of known camera GPS x, y, and z locations in relation to the location of the target feature helps to reduce scaling errors. Each FLIR survey attempted to make some dome measurements from viewpoints perpendicular to dome axis of interest (Fig. 21A). Estimating dome height from oblique FLIR views was least constrained. Height was estimated using the vertical component of the slope distance from dome base to the apex and the measured dome width (Fig. 21B).

Dimensions from both FLIR and satellite (see Section 4.2) compare well with derived DEM dome dimensions from Diefenbach et al. (2013). Day and night high-resolution satellite data also provided several dates with useful lava dome x and y dimensions (Figs. 14A, B, and 16B). The estimated z-value (height) from the nearest FLIR survey was used for volume estimates. FLIR and satellite derived volume estimates from several early dates (Fig. 22) are about 20–25% less than the photogrammetry-derived volumes from Diefenbach et al. (2013).

All of the photogrammetry-derived DEM volumes use the 16 April dome base elevation for each date beginning 16 April and after (Diefenbach et al., 2013), while the FLIR height estimates were measured from the visible dome base for each survey date. The difference in assumed base elevations and oblique dome height estimates combined with the half-ellipsoid dome shape approximation are likely the two main sources of volume error in the described FLIR and satellite volume method.

## 6. Conclusions

Regular high-resolution TIR imaging at active volcanoes is useful for monitoring and measuring lava flows and domes at many volcanoes around the world. Details of lava flow structure, texture, temperatures, and emissions are easily tracked using a variety of resolutions of spaceborne and airborne TIR data. While spaceborne TIR can provide a consistent, long-term synoptic view of a volcano's or arc's geothermal and eruptive activity, field-based TIR sensors are critical for validating the satellite observations and for collecting TIR data at a much higher spatial and temporal resolution than spaceborne systems. This study typically resulted in satellite-derived temperatures that were within error of the higher-resolution FLIR temperatures.

High-resolution TIR imaging is also essential for monitoring of low-temperature thermal features and detecting subtle changes over time. Retrospective analysis of archived high-resolution satellite TIR data was able to detect subtle, small-scale changes in thermal activity up to 16 months before the 2009 eruption of Redoubt Volcano. While infrequent ASTER TIR datasets were able to detect these subtle anomalies, robust, automated detection and early identification of thermal precursors at active volcanoes requires new high resolution multispectral TIR satellite sensors with frequent, at least daily, night and day acquisitions.

Supplementary materials related to this article can be found online at http://dx.doi.org/10.1016/j.jvolgeores.2012.04.014.

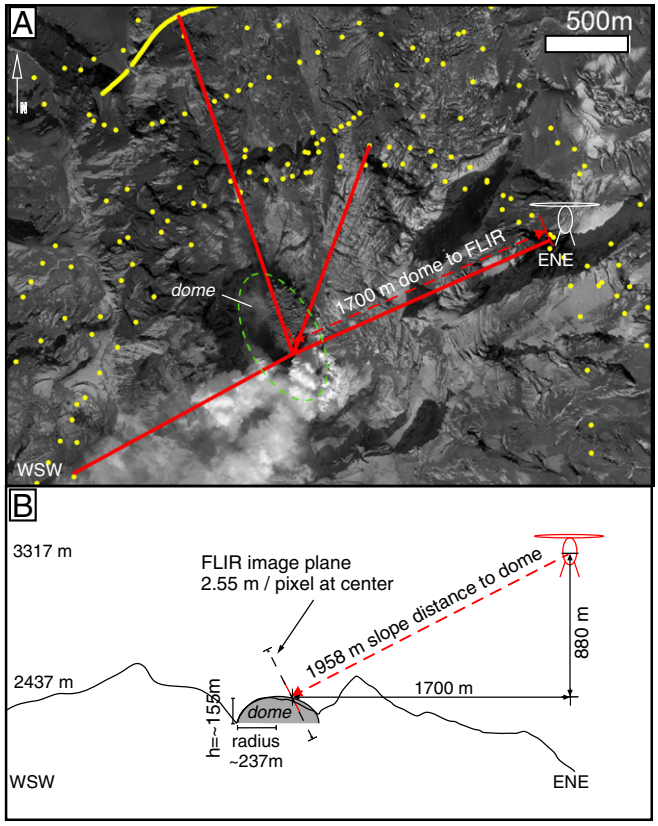


**Fig. 21.** (A.) Map of dome viewing positions for the 16 May FLIR survey with GPS points plotted on a 17 May 2009 WorldView-1 image (Copyright 2009 Digital Globe, Inc). Each line represents the map distance from the observer to the apex of the dome. (B) Scaled cross-section showing typical scenario for deriving FLIR image scales and dome dimension estimates from given helicopter locations.
Topographic profile extracted from 16 May 2009 DEM compiled by Diefenbach et al. (2013).

## Acknowledgments

Thanks to Alaska Volcano Observatory staff and students for their astute observations and insights during and after the 2009 Redoubt Volcano eruption. We express a special thank you to Kate Bull, Heather Bleick, Game McGimsey, Angie Diefenbach, and Cyrus Read for taking many amazing over flight photos and contributing useful discussions insights during this work. We thank Sonia Calvari and an anonymous reviewer for their helpful reviews. Thanks to Jon Dehn for his assistance and use of a FLIR S40 during the initial response. This work was funded by the U.S. Geological Survey Volcano Science Center. NASA (grant # NNH08AH80I) funding of the ASTER URP project (PI — Mike Ramsey, U. Pittsburgh) provided scheduling and rapid access to ASTER data and coordination with the ASTER Science Team. ASTER data were obtained courtesy of NASA/GSFC/METI/ERSDAC/JAROS and U.S./Japan ASTER Science Team. Thank you to the USGS EROS Landsat team for scheduling special winter day and night acquisitions from TM and ETM+ and Chris Noyles and Brenda Ellis for scheduling and acquiring a large variety of frequent, high-resolution commercial satellite data through NGA under Nextview licensing. RADARSAT-2 Data and Products © MacDONALD, DETTWILER AND ASSOCIATES LTD. 2009 — All Rights Reserved. RADARSAT is an official mark of the Canadian Space Agency.

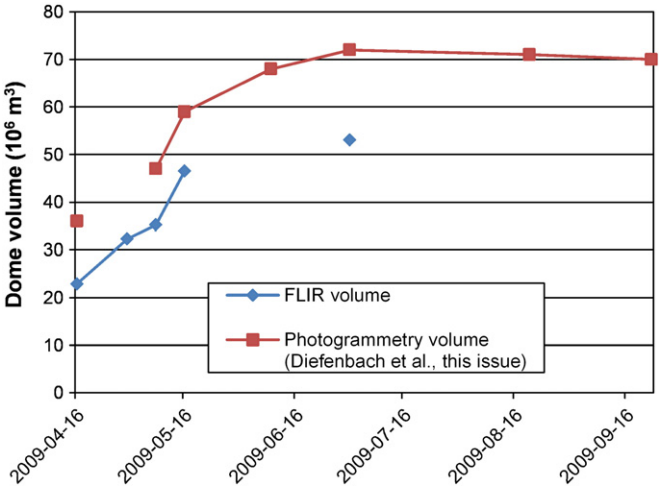


**Fig. 22.** Time series plot of FLIR-derived volumes from early in the extrusion of the final dome and photogrammetry-derived volumes (Diefenbach et al., 2013) throughout the final dome extrusion.

## References

Baldridge, A.M., Hook, S.J., Grove, C.I., Rivera, G., 2009. The ASTER spectral library version 2.0. Remote Sensing of Environment 113 (4), 711–715.
Ball, M., Pinkerton, H., 2006. Factors affecting the accuracy of thermal imaging cameras in volcanology. Journal of Geophysical Research 111 (B11), 1–14.
Bleick, H.A., Coombs, M.L., Cervelli, P.F., Bull, K., Wessels, R., 2013. Volcano–ice interactions precursory to the 2009 eruption of Redoubt Volcano, Alaska. Journal of Volcanology and Geothermal Research 259, 373–388.
Brantley, S.R., 1990. The eruption of Redoubt Volcano, Alaska, December 14, 1989–August 31, 1990. U.S. Geological Survey Circular, 1061. 33 pp.
Bull, K., Buurman, H., 2013. An overview of the 2009 eruption of Redoubt Volcano, Alaska. Journal of Volcanology and Geothermal Research 259, 2–15.
Bull, K.F., Anderson, S.W., Diefenbach, A.K., Wessels, R.L., Henton, S.M., 2013. Emplacement of the final lava dome of the 2009 eruption of Redoubt Volcano, Alaska. Journal of Volcanology and Geothermal Research 259, 334–348.
Buurman, H., West, M.E., Thompson, G., 2013. The seismicity of the 2009 Redoubt eruption. Journal of Volcanology and Geothermal Research 259, 16–30.
Calvari, S., Spampinato, L., Lodato, L., Harris, A.J.L., Patrick, M.R., Dehn, J., Burton, M.R., Andronico, D., 2005. Chronology and complex volcanic processes during the 2002–2003 flank eruption at Stromboli volcano (Italy) reconstructed from direct observations and surveys with a handheld thermal camera. Journal of Geophysical Research 110 (B2), 1–23.
Carter, A.J., Ramsey, M.S., 2009. ASTER- and field-based observations at Bezymianny Volcano: focus on the 11 May 2007 pyroclastic flow deposit. Remote Sensing of Environment 113, 2142–2151.
Carter, A.J., Ramsey, M.S., 2010. Long-term volcanic activity at Shiveluch Volcano: nine years of ASTER spaceborne thermal infrared observations. Remote Sensing 2 (11), 2571–2583.
Carter, A.J., Ramsey, M.S., Belousov, A.B., 2007. Detection of a new summit crater on Bezymianny Volcano lava dome: satellite and field-based thermal data. Bulletin of Volcanology 69 (9), 811–815.
Coombs, M.L., Sisson, T.W., Bleick, H.A., Henton, S.M., Nye, C.J., Payne, A.L., Cameron, C.E., Larsen, J.F., Wallace, K.L., Bull, K.F., 2013. Andesites of the 2009 eruption of Redoubt Volcano, Alaska. Journal of Volcanology and Geothermal Research 259, 349–372.
Coppola, D., James, M.R., Staudacher, T., Cigolini, C., 2010. A comparison of field- and satellite-derived thermal flux at Piton de la Fournaise: implications for the calculation of lava discharge rate. Bulletin of Volcanology 72, 341–356.
Davies, A.G., Calkins, J., Scharenbroich, L., Vaughan, R.G., Wright, R., Kyle, P., Castaño, R., Chien, S., Tran, D., 2008. Multi-instrument remote and in situ observations of the Erebus Volcano (Antarctica) lava lake in 2005: a comparison with the Pele lava lake on the Jovian moon Io. Journal of Volcanology and Geothermal Research 177 (3), 705–724.
Diefenbach, A.K., Bull, K.F., Wessels, R.L., McGimsey, R.G., 2013. Photogrammetric monitoring of lava dome growth during the 2009 eruption of Redoubt Volcano. Journal of Volcanology and Geothermal Research 259, 308–316.
Dozier, J., 1981. A method for satellite identification of surface temperature fields of subpixel resolution. Remote Sensing of Environment 11, 221–229.
Duda, K.A., Ramsey, M., Wessels, R., Dehn, J., 2009a. Optical satellite volcano monitoring: a multi-sensor rapid response system. Geoscience and Remote Sensing 1–24.
Duda, K.A., Ramsey, M.S., Wessels, R.L., Dehn, J., 2009b. Optical satellite volcano monitoring —a multi-sensor rapid response system. In: Ho, P.-G.P. (Ed.), Geoscience and Remote Sensing. InTech, Vukovar, Croatia, pp. 473–496.
Flynn, L.P., Mouginis-Mark, P.J., Horton, K.A., 1994. Distribution of thermal areas on active lava flow field: Landsat observations of Kilauea, Hawaii, July 1991. Bulletin of Volcanology 56, 284–296.
Gillespie, A.R., Rokugawa, S., Matsunaga, T., Cothern, J.S., Hook, S.J., Kahle, A.B., 1998. A temperature and emissivity separation algorithm for Advanced Spaceborne Thermal Emission and Reflection Radiometer (ASTER) images. Institute of Electrical and Electronics Engineers Transactions Geoscience Remote Sensing 36, 1113–1126.
Harris, A.J.L., Stevenson, D.S., 1997. Thermal observations of degassing open conduits and fumaroles at Stromboli and Vulcano using remotely sensed data. Journal of Volcanology and Geothermal Research 76, 175–198.

Harris, A.J.L., Flynn, L.P., Keszthelyi, L., Mouginis-Mark, P.J., Rowland, S.K., Resing, J.A., 1998. Calculation of lava effusion rates from Landsat TM data. Bulletin of Volcanology 60, 52–71.
Harris, A.J.L., Flynn, L.P., Rothery, D.A., Oppenheimer, C., Sherman, S.B., 1999. Mass flux measurements at lava lakes: implications for magma recycling. Journal of Geophysical Research 104, 7117–7136.
Harris, A.J.L., Flynn, L.P., Matías, O., Rose, W.I., 2002. The thermal stealth flows of Santiaguito: implications for the cooling and emplacement of dacitic block lava flows. Geological Society of America Bulletin 114, 533–546.
Harris, A.J.L., Rose, W.I., Flynn, L.P., 2003. Temporal trends in lava dome extrusion at Santiaguito 1922–2000. Bulletin of Volcanology 65, 77–89.
Harris, A.J.L., Dehn, J., Patrick, M., Calvari, S., Ripepe, M., Lodato, L., 2005. Lava effusion rates from hand-held thermal infrared imagery; an example from the June 2003 effusive activity at Stromboli. Bulletin of Volcanology 68, 107–117.
Kaneko, T., Wooster, M.J., Nakada, S., 2002. Exogenous and endogenous growth of the Unzen lava dome examined by satellite infrared image analysis. Journal of Volcanology and Geothermal Research 116, 151–160.
Kervyn, M., Harris, A.J.L., Belton, F., Mbede, E., Jacobs, P., Ernst, G.G.J., 2008. Thermal remote sensing of the low-intensity carbonatite volcanism of Oldoinyo Lengai, Tanzania. International Journal of Remote Sensing 29, 6467–6499.
Lombardo, V., Buongiorno, M.F., Pieri, D., Merucci, L., 2004. Differences in Landsat TM derived lava flow thermal structures during summit and flank eruption at Mount Etna. Journal of Volcanology and Geothermal Research 134, 15–34.
Lopez, T., Carn, S., Werner, C., Fee, D., Kelly, P., Doukas, M., Pfeffer, M., Webley, P., Cahill, C., Schneider, D., 2013. Evaluation of Redoubt Volcano's sulfur dioxide emissions by the Ozone Monitoring Instrument. Journal of Volcanology and Geothermal Research 259, 290–307.
Miller, T.P., 1994. Dome growth and destruction during the 1989–1990 eruption of Redoubt Volcano. Journal of Volcanology and Geothermal Research 62 (1–4, Special Issue), 197–212.
Miller, T.P., Chouet, B.A., 1994. The 1989–1990 eruptions of Redoubt Volcano: an introduction. Journal of Volcanology and Geothermal Research 62 (1–4, Special Issue), 1–10.
Oppenheimer, C., 1993. Thermal distributions of hot volcanic surfaces constrained using three infrared bands of remote sensing data. Geophysical Research Letters 20 (6), 431–434.
Oppenheimer, C., Yirgu, G., 2002. Thermal imaging of an active lava lake: Erta 'Ale volcano, Ethiopia. International Journal of Remote Sensing 23 (22), 4777–4782.
Patrick, M., Dean, K., Dehn, J., 2004. Active mud volcanism observed with Landsat 7 ETM+. Journal of Volcanology and Geothermal Research 131, 307–320.
Patrick, M.R., Kauahikaua, J.P., Antolik, L., 2010. MATLAB tools for improved characterization and quantification of volcanic incandescence in Webcam imagery; applications at Kīlauea Volcano, Hawai'i. U.S. Geological Survey Techniques and Methods 13, A1 16 pp.
Pieri, D.C., Abrams, M.J., 2005. ASTER observations of thermal anomalies preceding the April 2003 eruption of Chikurachki Volcano, Kurile Islands, Russia. Remote Sensing of Environment 99, 84–94.
Planck, M., 1914. The Theory of Heat Radiation. Translated into English by M. Masius Second edition. Blakiston's Son & Co., Philadelphia. reprinted by Kessinger, 225 pp.
Ramsey, M., Dehn, J., 2004. Spaceborne observations of the 2000 Bezymianny, Kamchatka eruption; the integration of high-resolution ASTER data into near real-time monitoring using AVHRR. Journal of Volcanology and Geothermal Research 135 (1–2), 127–146.
Rothery, D.A., Francis, P.W., Wood, C.A., 1988. Volcano monitoring using short wavelength infrared data from satellites. Journal of Geophysical Research 93 (B7), 7993–8008.
Sahetapy-Engel, S.T., Harris, A.J.L., 2009. Thermal structure and heat loss at the summit crater of an active lava dome. Bulletin of Volcanology 71, 15–28.
Sawyer, G.M., Burton, M.R., 2006. Effects of a volcanic plume on thermal imaging data. Geophysical Research Letters 33, L14311. http://dx.doi.org/10.1029/2005GL025320.
The 2009 eruption of Redoubt Volcano. In: Schaefer, J.R. (Ed.), Alaska, Alaska Division of Geological & Geophysical Surveys Report of Investigation 2012–5. 45 pp.
Schneider, D.J., Hoblitt, R.P., 2013. Doppler weather radar observations of the 2009 eruption of Redoubt Volcano, Alaska. Journal of Volcanology and Geothermal Research 259, 133–144.
Schneider, D., Vallance, J., Wessels, R., Logan, M., Ramsey, M., 2009. Use of thermal infrared imaging for monitoring renewed dome growth at Mount St. Helens, 2004. In: Sherrod, D.R., Scott, W.E., Stauffer, P.H. (Eds.), A Volcano Rekindled; the Renewed Eruption of Mount St. Helens, 2004–2006. USGS Prof. Paper 1750, pp. 347–359.
Spampinato, L., Calvari, S., Oppenheimer, C., Boschi, E., 2011. Volcano surveillance using infrared cameras. Earth-Science Reviews 106, 63–91.
Thome, K., Palluconi, F., Takashima, T., Masuda, K., 1998. Atmospheric correction of ASTER. Institute of Electrical and Electronics Engineers Transactions on Geoscience and Remote Sensing 36 (4), 1199–1211.
Till, A.B., Yount, M.E., Bevier, M.L., 1994. The geologic history of Redoubt Volcano, Alaska. Journal of Volcanology and Geothermal Research 62, 11–30.
Trunk, L., Bernard, A., 2008. Investigating crater lake warming using ASTER thermal imagery: case studies at Ruapehu, Poás, Kawah Ijen, and Copahué Volcanoes. Journal of Volcanology and Geothermal Research 178, 259–270.
Vaughan, R.G., Hook, S.J., 2006. Using satellite data to characterize the temporal thermal behavior of an active volcano; Mount St. Helens, WA. Geophysical Research Letters 33, L20303. http://dx.doi.org/10.1029/2006GL027957.
Vaughan, R.G., Hook, S.J., Ramsey, M.S., Realmuto, V.J., Schneider, D.J., 2005. Monitoring eruptive activity at Mount St. Helens with TIR image data. Geophysical Research Letters 32, L19305. http://dx.doi.org/10.1029/2005GL024112.
Vaughan, R.G., Keszthelyi, L.P., Davies, A.G., Schneider, D.J., Jaworowski, C., Heasler, H., 2010. Exploring the limits of identifying sub-pixel thermal features using ASTER TIR data. Journal of Volcanology and Geothermal Research 189 (3–4), 225–237.
Wallace, K.L., Schaefer, J.R., Coombs, M.L., 2013. Character, mass, distribution, and origin of tephra-fall deposits from the 2009 eruption of Redoubt Volcano, Alaska—Highlighting the significance of particle aggregation. Journal of Volcanology and Geothermal Research 259, 145–169.
Waythomas, C., Pierson, T., Major, J.J., Scott, W.E., 2013. Voluminous ice-rich and water-rich lahars generated during the 2009 eruption of Redoubt Volcano, Alaska. Journal of Volcanology and Geothermal Research 259, 389–413.
Webley, P.W., Lopez, T.M., Ekstrand, A.L, Dean, K.G., Rinkleff, P., Dehn, J., Cahill, C.F., Wessels, R.L., Bailey, J.E., Izbekov, P., Worden, A., 2013. Remote observations of eruptive clouds and surface thermal activity during the 2009 eruption of Redoubt Volcano. Journal of Volcanology and Geothermal Research 259, 185–200.
Werner, C., Kelly, P.J., Doukas, M., Lopez, T., Pfeffer, M., McGimsey, R., Neal, C., 2013. Degassing of $CO_2$, $SO_2$, and $H_2S$ associated with the 2009 eruption of Redoubt Volcano, Alaska. Journal of Volcanology and Geothermal Research 259, 270–284.
Wessels, R.L., Coombs, M.L., Schneider, D.J., Dehn, J., Ramsey, M.S., 2010. High-resolution satellite and airborne thermal infrared imaging of the 2006 eruption of Augustine Volcano. In: Power, J.A., Coombs, M.L., Freymueller, J.T. (Eds.), The 2006 Eruption of Augustine Volcano, Alaska. USGS Prof. Paper 1769, pp. 527–552.
Wooster, M.J., Kaneko, T., Nakada, S., Shimizu, H., 2000. Discrimination of lava dome activity styles using satellite-derived thermal structures. Journal of Volcanology and Geothermal Research 102, 97–118.
Wright, R., Flynn, L., 2003. On the retrieval of lava-flow surface temperatures from infrared satellite data. Geology 31, 893–896.
Yamaguchi, Y., Kahle, A.B., Tsu, H., Kawakami, T., Pniel, M., 1998. Overview of Advanced Spaceborne Thermal Emission and Reflection Radiometer (ASTER). Institute of Electrical and Electronics Engineers Transactions Geoscience Remote Sensing 36 (4), 1062–1071.
Young, K.D., Loughlin, S., Ryan, G., Voight, B., Hards, V., 2007. Ground-based thermal infrared monitoring of dome growth at Soufriere Hills Volcano, Montserrat. American Geophysical Union Fall Meeting abstract V21A-0389.